Stellar contents and star formation in the young open cluster Stock 8

Jessy Jose,[1]★ A. K. Pandey,[1,2,3] D. K. Ojha,[3] K. Ogura,[4] W. P. Chen,[2] B. C. Bhatt,[5] S. K. Ghosh,[3] H. Mito,[6] G. Maheswar[1,7] and Saurabh Sharma[1]

[1]*Aryabhatta Research Institute of Observational Sciences (ARIES), Manora Peak, Nainital 263129, India*
[2]*Institute of Astronomy, National Central University, Chung-Li 32054, Taiwan*
[3]*Tata Institute of Fundamental Research, Mumbai 400005, India*
[4]*Kokugakuin University, Higashi, Shibuya-ku, Tokyo 150-8440, Japan*
[5]*CREST, Indian Institute of Astrophysics, Koramangala, Bangalore 560034, India*
[6]*Kiso Observatory, School of Science, University of Tokyo, Mitake-mura, Kiso-gun, Nagano 397-0101, Japan*
[7]*Korea Astronomy and Space Science Institute (KASI), 61-1 Hwaam-dong, Yuseong-gu, Daejeon 305-348, Korea*

ABSTRACT

We present $UBVI_c$ CCD photometry of the young open cluster Stock 8 with the aim of studying its basic properties such as the amount of interstellar extinction, distance, age, stellar contents and initial mass function (IMF). We also studied the star formation scenario in this region. From optical data, the radius of the cluster is found to be ∼6 arcmin (∼3.6 pc) and the reddening within the cluster region varies from $E(B - V) = 0.40$ to 0.60 mag. The cluster is located at a distance of 2.05 ± 0.10 kpc. Using Hα slitless spectroscopy and Two Micron All Sky Survey (2MASS) near-infrared (NIR) data we identified Hα emission and NIR-excess young stellar objects (YSOs), respectively. From their locations in the colour–magnitude diagrams, majority of them seem to have ages between 1 and 5 Myr. The spread in their ages indicate a possible non-coeval star formation in the cluster. Massive stars in the cluster region reveal an average age of $\leqslant 2$ Myr. In the cluster region ($r \leqslant 6$ arcmin) the slope of the mass function (MF), Γ, in the mass range ∼$1.0 \leqslant M/M_{\odot} < 13.4$ can be represented by a power law having a slope of -1.38 ± 0.12, which agrees well with Salpeter value (-1.35). In the mass range $0.3 \leqslant M/M_{\odot} < 1.0$, the MF is also found to follow a power law with a shallower slope of $\Gamma = -0.58 \pm 0.23$ indicating a break in the slope of the IMF at ∼1 $M_{\odot}$. The slope of the K-band luminosity function for the cluster ($r \leqslant 6$ arcmin) is found to be 0.31 ± 0.02, which is smaller than the average value (∼0.4) obtained for embedded star clusters.

A significant number of YSOs are distributed along a Nebulous Stream towards the east side of the cluster. A small cluster is embedded in the Nebulous Stream. The YSOs lying in the Nebulous Stream and in the embedded cluster are found to be younger than the stars in the cluster Stock 8. The radio continuum, *MSX*, *IRAS* mid- and far-infrared maps and the ratio of [S II]/Hα intensities indicate that the eastern region of Stock 8 is ionization bounded whereas the western region is density bounded. The morphology seems to indicate that the ionization/shock front caused by the ionizing sources located in the Stock 8 region and westwards of Stock 8 has not reached the Nebulous Stream. It appears that star formation activity in the Nebulous Stream and embedded cluster may be independent from that of Stock 8.

Key words: stars: formation – stars: luminosity function, mass function – stars: pre-main-sequence – open clusters and associations: individual: Stock 8.

1 INTRODUCTION

The study of star formation process and stellar evolution constitute one of the basic problems in astrophysics. Since most of the stars tend to form in clusters or groups, star clusters are useful objects to study the star formation process. The initial mass function (IMF), defined as the distribution of stellar masses at the time of birth is one of the basic tools for understanding the formation and evolution of stellar systems. Star-forming regions (SFRs) and young star clusters have proven to be the ideal laboratories for studying the form of IMF and its variation through space and time. Since the young clusters (age <10 Myr) are assumed to be less affected by

★E-mail: jessy@aries.ernet.in

dynamical evolution, their mass function (MF) can be considered as the IMF. However, a recent study by Kroupa (2007) argues that even in the youngest clusters, it is difficult to trace the IMF, as clusters evolve rapidly and therefore eject a fraction of their members even at a very young age.

There are many unsolved issues concerning the universality of the stellar IMF. The theoretical expectation is that the IMF of a cluster should depend on the location, size, metallicity, density of the star-forming environment and other conditions such as temperature or pressure (Larson 1992; Price & Podsiadlowski 1995). However, convincing evidence for variation in the stellar IMF has not yet been found observationally (Scalo 1998; Kroupa 2001, 2002). Massey, Johnson & Degio-Eastwood (1995) concluded that the slope of the IMF at the higher mass range is universal, with a value of $\Gamma = -1.1 \pm 0.1$ irrespective of the variations in metallicity. Luhman et al. (2000) also found no systematic variations in IMF of the nearby SFRs (such as ρ Oph, IC 348, Trapezium) although there is a large difference in stellar densities. On the other hand Hillenbrand (1997) found a few SFRs with unusual IMFs.

The lack of strong evidence for IMF variations suggests that its fundamental form may be universal. Consequently, local conditions may not play any significant role in the star formation process. However, the influence of star formation history of young clusters on the form of IMF is still an open issue. High-mass stars have strong influence on their surroundings and can significantly affect the formation of low-mass stars. Recently, a relatively large number of low-mass stars have been detected in a few OB associations, e.g. Upper Scorpio, the σ and λ Ori regions (Preibisch & Zinnecker 1999; Dolan & Mathieu 2002). Since this realization, surveys have demonstrated that the IMFs must essentially be the same in all SFRs. The apparent difference is due mainly to the inherent low percentage of high-mass stars and the incomplete survey of low-mass stars in high-mass SFRs (e.g. Massey et al. 1995; Hillenbrand 1997; Preibisch & Zinnecker 1999). Recently Parker & Goodwin (2007) have studied the origin of O stars and their effect on low-mass star formation. Advancement in detectors along with various surveys such as the Two Micron All Sky Survey (2MASS), DENIS and available archived data from *ISO* and *Spitzer* space telescopes have permitted detailed studies of low-mass stellar population in regions of high-mass star formation.

With the aim of understanding the star formation process and IMF in and around young star cluster regions containing OB stars, we selected young cluster Stock 8 located within the H II region of IC 417 (Sh2-234) in the Auriga constellation of the Perseus arm. No CCD photometric observations have been carried out for this region so far. Mayer & Macak (1971) have carried out photoelectric photometry of 11 bright stars in the region and reported a distance of 2.96 kpc for the cluster. Using the photographic study of stars brighter than $V = 16$ mag, Malysheva (1990) found cluster age as $\sim$12 Myr with an angular diameter of 20 arcmin and a distance of 1.9 kpc.

The present study is an attempt to understand the structure, star formation history, pre-main-sequence (PMS) population and the form of IMF of Stock 8 using the $UBVI_c$ CCD photometry data. In Sections 2 and 3, we describe the observations, data reductions and archived data used in the present work. Sections 4–8 describe various results. The star formation scenario in the IC 417 (Sh2-234) region is described in Sections 9–12. The results are summarized in Section 13.

2 OBSERVATIONS AND DATA REDUCTIONS

The 30×30 arcmin^2 ($\sim$17.9 $\times$ 17.9 pc^2) area containing the central region of Stock 8, reproduced from the DSS2 *R*-band image, is shown in Fig. 1. As evident from the figure, Stock 8 is embedded in an H II region. To the west of it, there are several OB stars which appear to form an OB association. To the east of Stock 8, we find a very peculiar chord-like nebulosity which we term as Nebulous Stream. A small cluster is also embedded within the Nebulous Stream. The small embedded cluster and the Nebulous Stream are discussed in Sections 9 and 11, respectively. We describe below the observations made to carry out a detailed study of the region.

2.1 Optical CCD photometry

The CCD $UBVI_c$ observations were carried out using the 2048 $\times$ 2048 pixel CCD camera on the 105-cm Schmidt telescope of the Kiso Observatory, Japan on 2004 November 4. At the Schmidt focus (f/3.1) each pixel of 25 μm corresponds to 1.5 arcsec and the entire chip covers a field of $\sim$ 50 $\times$ 50 arcmin^2 on the sky. The readout noise and gain of the CCD are 23.2 e$^-$ and 3.4 e$^-$ ADU^{-1}, respectively. The full width at half-maximum (FWHM) of the star images was $\sim$3 arcsec. A number of bias and dome flat frames were also taken during the observing runs. We took short and long exposures in all the filters to avoid saturation of bright stars. SA 92 field of Landolt (1992) was observed to standardize the field on the same night. The log of observations is tabulated in Table 1.

The CCD frames were bias-subtracted and flat-field corrected in the standard manner using various tasks available under IRAF.[1] Aperture photometry was done for the standard stars of SA 92 field to estimate the atmospheric extinction and to calibrate the field. Following calibration equations are derived using a least-squares linear regression:

$$(U - B) = (0.887 \pm 0.025)(u - b) - (2.973 \pm 0.010),$$
$$(B - V) = (1.233 \pm 0.009)(b - v) + (0.482 \pm 0.010),$$
$$(V - I) = (0.847 \pm 0.008)(v - i) + (0.758 \pm 0.006),$$
$$V = v - (0.095 \pm 0.008)(V - I) - (2.578 \pm 0.007),$$

where u, b, v, i are the instrument magnitudes corrected for the atmospheric extinctions and U, B, V, I are the standard magnitudes. Fig. 2 shows the standardization residuals, Δ, between standard and transformed V magnitudes, $(U - B)$, $(B - V)$ and $(V - I)$ colours of standard stars as a function of V magnitude. The standard deviations in ΔV, $\Delta(U - B)$, $\Delta(B - V)$ and $\Delta(V - I)$ are 0.021, 0.045, 0.023, 0.015 mag, respectively.

Different frames of cluster region of same exposure time and filters were averaged. Photometry of cleaned frames was carried out using the DAOPHOT-II (Stetson 1987) profile-fitting software. The magnitudes of bright stars were taken from short exposure frames whereas that of faint stars were taken from deep exposures. Profile-fitting photometry gives the error in magnitude determination, the goodness-of-fit parameter, χ, which is a measure of the average rms deviation to the point spread function (PSF) fit normalized to the expected errors. It also gives a shape parameter, Sharpness, which measures how well the PSF fits the object. The photometric errors in magnitude, colours and image parameters as a function of V magnitude are shown in Fig. 3. These parameters were used to reject poor measurements.

Deep images of two central regions of the cluster and a nearby field ($\alpha_{2000} = 05^h29^m42^s$; $\delta_{2000} = +34°42'13''$) were also obtained in V and I_c filters on 2006 September 29 using a 1024 $\times$ 1024 pixel CCD camera mounted at the f/13 Cassegrain focus of the 104-cm Sampurnanand Telescope (ST) of the Aryabhatta Research Institute of Observational Sciences (ARIES), Nainital, India. Log of the

---

[1] IRAF is distributed by National Optical Astronomy Observatories, USA.
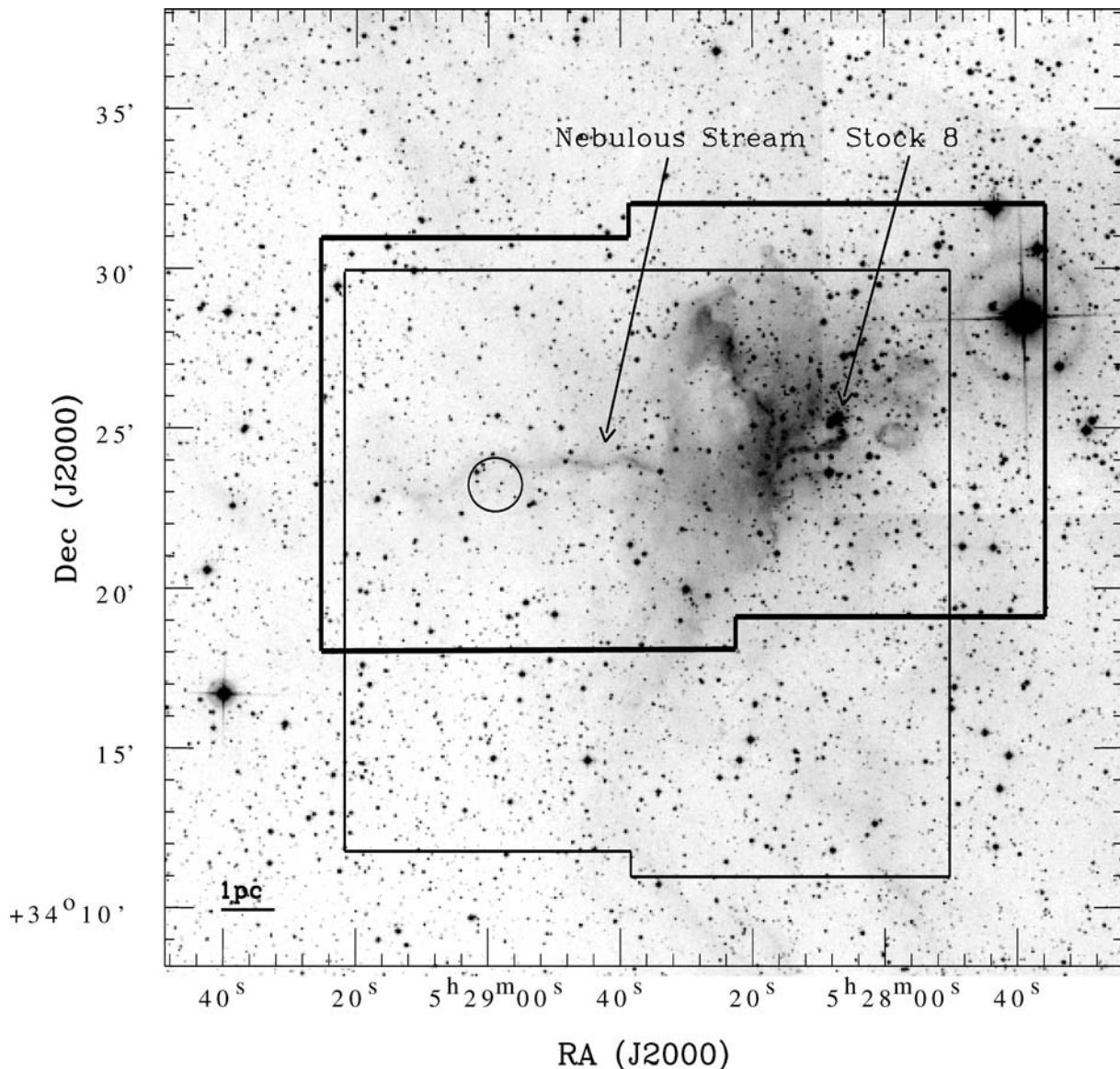
Figure 1. The 30×30 arcmin^2 DSS2 *R*-band image of the region around Stock 8. The area marked with thin lines is the region covered by slitless spectroscopic observations and the area marked with thick lines is the region for which deep images are taken in *V* and I_c bands. The circle represents the location of the small embedded cluster (see Section 9). Locations of the Nebulous Stream (see Section 11) and Stock 8 are also marked. The abscissa and the ordinates are for J2000 epoch.

observations is given in Table 1. In this set-up, each pixel of the CCD corresponds to 0.37 arcsec and the entire chip covers a field of $\sim 13 \times 13$ arcmin^2 on the sky. To improve the signal-to-noise ratio (S/N), the observations were carried out in binning mode of 2×2 pixel. The FWHM of the star images was ~ 1.8 arcsec. The observed region is marked by thick lines in Fig. 1. The secondary standards from the Kiso observations were used to calibrate the data taken at ARIES. The typical DAOPHOT photometric errors at brighter end ($V \sim 15$) are of the order of ~ 0.01 mag, whereas the errors increase towards the fainter end (~ 0.05 at $V \sim 21$). The combined photometric data of Kiso Schmidt telescope and ST in an area of 40×40 arcmin^2 along with positions of the stars are given in a table, which is only available in electronic form as part of the online material from http://www.blackwell-synergy.com. Format of the table is shown in Table 2.

To study the luminosity function (LF)/MF it is necessary to take into account the incompleteness in the observed data that may occur for various reasons (e.g. crowding of the stars). A quantitative evaluation of the completeness of the photometric data with respect to the brightness and the position on a given frame is necessary to convert the observed LF to a true LF. We used the ADDSTAR routine of DAOPHOT-II to determine the completeness factor (CF). The procedure has been outlined in detail in our earlier work (Pandey et al. 2001). Briefly, we randomly added artificial stars to both *V* and *I* images in such a way that they have similar geometrical locations but differ in *I* brightness according to mean $(V - I)$ colour (~ 1.5) of the data sample. The luminosity distribution of artificial stars is chosen in such a way that more stars are inserted towards the fainter magnitude bins. The frames are reduced using the same procedure used for the original frame. The ratio of the number of

Table 1. Log of observations.

α (2000) (h:m:s)	δ (2000) (° : ′ : ″)	Date of observation	Filter	Exposure time (s) × no. of frames
Kiso[a]				
05:28:07	+34:25:42	2004.11.04	U	60 × 3, 180 × 4
05:28:07	+34:25:42	2004.11.04	B	20 × 4, 60 × 4
05:28:07	+34:25:42	2004.11.04	V	10 × 4, 60 × 4
05:28:07	+34:25:42	2004.11.04	I_c	10 × 4, 60 × 4
ST[b]				
05:28:07	+34:25:35	2006.09.29	V	5 × 2, 300 × 3, 600 × 4
05:28:07	+34:25:35	2006.09.29	I_c	5 × 3, 120 × 5
05:28:54	+34:24:32	2006.09.29	V	5 × 2, 300 × 3, 600 × 4
05:28:54	+34:24:32	2006.09.29	I_c	5 × 3, 120 × 5
05:29:42	+34:42:13	2006.09.29	V	5 × 2, 300 × 3, 600 × 4
05:29:42	+34:42:13	2006.09.29	I_c	5 × 3, 120 × 5
HCT[c]				
05:28:14	+34:24:52	2005.09.26	Hα-Br	60 × 2
05:28:14	+34:24:52	2005.09.26	Gr5/Hα-Br	420 × 3
05:28:14	+34:15:55	2005.09.27	Hα-Br	60 × 3
05:28:14	+34:15:55	2005.09.27	Gr5/Hα-Br	420 × 3
05:28:56	+34:16:43	2005.10.10	Hα-Br	60 × 3
05:28:56	+34:16:43	2005.10.10	Gr5/Hα-Br	420 × 3
05:28:32	+34:29:55	2005.10.10	Hα-Br	60 × 3
05:28:32	+34:29:55	2005.10.10	Gr5/Hα-Br	420 × 3
05:28:07	+34:25:35	2006.09.24	Hα-Br	450 × 1
05:28:07	+34:25:35	2006.09.24	[S II]	450 × 1
05:28:07	+34:25:35	2006.09.24	R	450 × 1
05:28:47	+34:25:35	2006.09.24	Hα-Br	450 × 1
05:28:47	+34:25:35	2006.09.24	[S II]	450 × 1
05:28:47	+34:25:35	2006.09.24	R	450 × 1

[a]105-cm Schmidt Telescope, Kiso, Japan. [b]104-cm ST, ARIES, Nainital. [c]2-m Himalayan Chandra Telescope, IAO, Hanle.
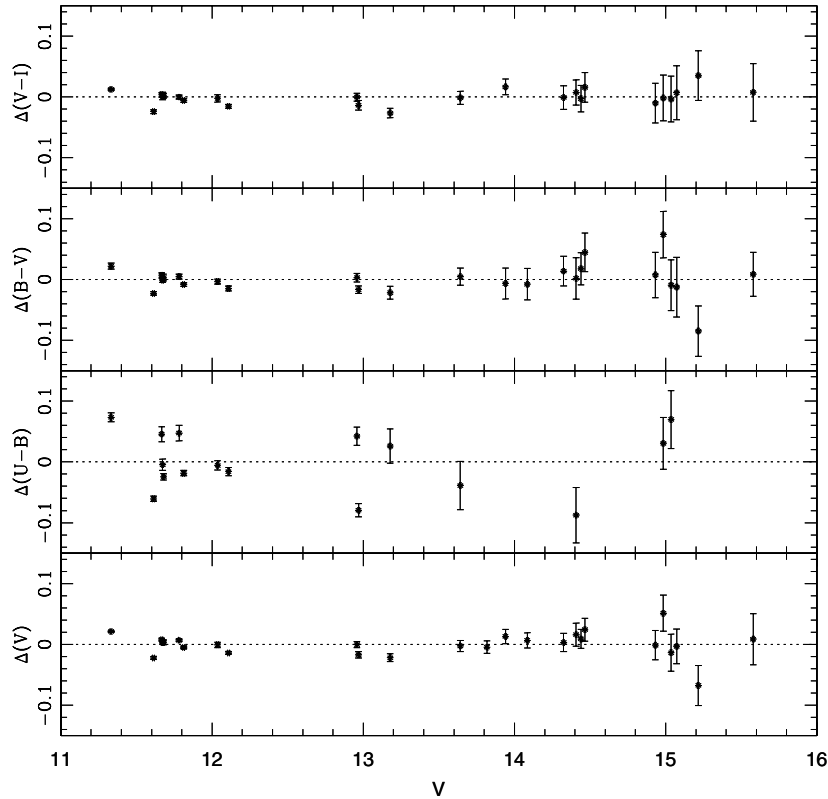
Figure 2. Residuals between standard and transformed magnitude and colours of standard stars plotted against the Landolt standard *V* magnitude. These observations are from Kiso Schmidt telescope. The error bars represent combined errors of Landolt (1992) and present measurements.
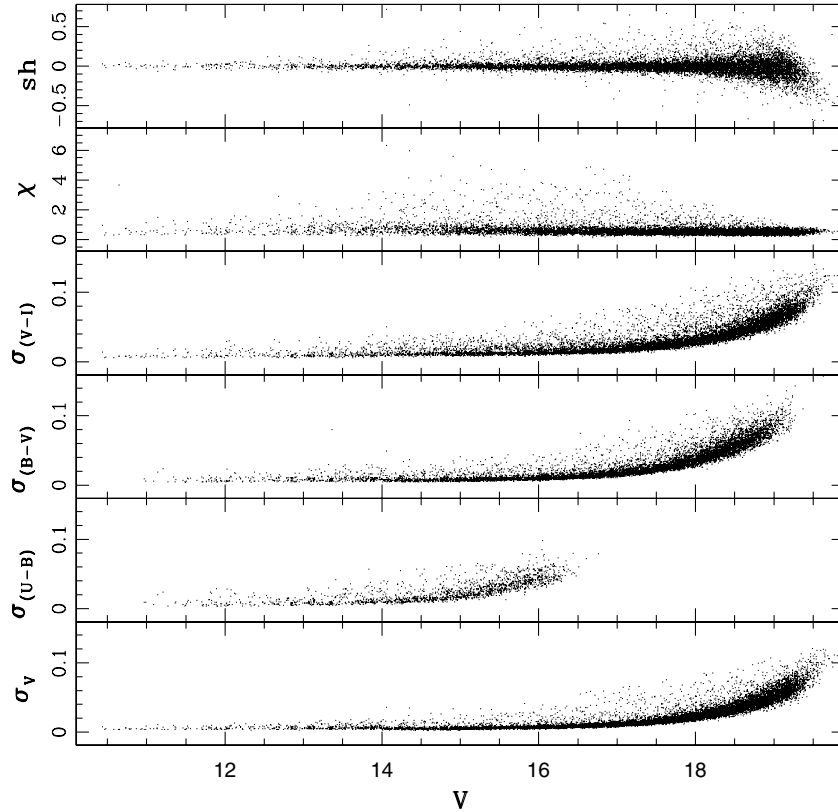
Figure 3. The photometric errors in V, $(U - B)$, $(B - V)$, $(V - I)$, image parameters χ and Sharpness as a function of V magnitude for Kiso observations.

Table 2. $UBVI_c$ photometric data of the sample stars. The complete table is available in electronic form only.

Star no.	α (2000) (h:m:s)	δ (2000) ($^\circ : ' : ''$)	V	$(U - B)$	$(B - V)$	$(V - I)$
1	05:27:48.31	+34:21:26.6	11.210	0.032	0.746	0.724
2	05:28:01.22	+34:27:00.7	11.498	0.129	0.174	0.281
3	05:27:43.61	+34:21:24.8	11.271	−0.481	0.417	0.617
4	05:28:50.26	+34:19:23.2	11.507	0.015	0.174	0.298
5	05:28:04.46	+34:29:20.8	11.710	−0.474	0.298	0.494

Table 3. CF of photometric data in the cluster and field regions.

V range (mag)	Stock 8 $r \leqslant 3$ arcmin	$3 < r \leqslant 6$ arcmin	Field region
10–11	1.00	1.00	1.00
11–12	1.00	1.00	1.00
13–14	1.00	1.00	1.00
14–15	1.00	1.00	1.00
15–16	1.00	1.00	1.00
16–17	0.98	0.97	0.98
17–18	0.95	0.95	0.97
18–19	0.93	0.93	0.96
19–20	0.88	0.90	0.92
20–21	0.88	0.86	0.86
21–22	0.74	0.75	0.76

stars recovered to those added in each magnitude interval gives the CF as a function of magnitude. The minimum value of the CF of the pair (i.e. V- and I-band observations) for the two subregions, given in Table 3, is used to correct the data for incompleteness. The incompleteness of the data increases with increasing magnitude as expected; however, it does not depend on the area significantly.

2.2 Slitless spectroscopy, Hα and [S II] imaging

The cluster was observed in slitless mode with grism as the dispersing element using the Himalaya Faint Object Spectrograph Camera (HFOSC) on the 2-m Himalayan Chandra Telescope (HCT) of Indian Astronomical Observatory (IAO), Hanle, India. The central 2048×2048 pixel of 2048×4096 CCD were used for data acquisition. The pixel size is 15 μm with an image scale of 0.296 arcsec pixel^{-1} and it covers an area of 10×10 arcmin^2 on the sky. A combination of Hα broad-band filter (Hα-Br; 6100–6740 Å) and Grism 5 were used without any slit. The resolution of Grism 5

is 870. The regions where slitless spectroscopic observations were carried out are identified with thin lines in Fig. 1. Emission-line stars with enhancement over the continuum at Hα wavelength are visually identified. Multiple frames were taken to confirm the presence of Hα-emitting sources. Positions of the Hα emission stars are given in Table 4. Hα-Br and [S II] ($\lambda = 6724$ Å, $\Delta\lambda \sim 100$ Å) images of two central regions of the cluster were also acquired on 2006 September 24 using the HFOSC at the 2-m HCT. Log of the observations is given in Table 1.

3 ARCHIVAL DATA

Near-infrared (NIR) JHK_s data for point sources within a radius of 20 arcmin around Stock 8 have been obtained from the 2MASS

Table 4. Coordinates and photometric data of detected Hα emission stars.

ID	α (2000) (h:m:s)	δ (2000) (° : ′ : ″)	V (mag)	B − V (mag)	V − I (mag)
1	05:28:04.65	+34:21:51.0	15.642	0.961	1.205
2	05:28:00.00	+34:24:40.5	19.522	–	1.728
3	05:28:00.45	+34:25:57.8	18.493	1.594	2.030
4	05:28:06.09	+34:24:55.4	18.084	–	1.460
5	05:28:06.90	+34:24:49.6	14.800	0.970	1.285
6	05:28:05.72	+34:25:28.1	17.108	–	1.778
7	05:28:08.65	+34:25:38.9	16.700	1.218	1.812
8	05:28:16.07	+34:27:28.8	18.284	1.379	2.125
9	05:28:17.12	+34:28:04.1	15.565	1.249	1.568
10	05:28:25.90	+34:23:10.2	16.467	0.852	1.161
11	05:28:35.83	+34:24:32.8	15.267	1.256	1.694
12	05:28:18.22	+34:16:52.7	16.486	1.144	1.337
13	05:28:34.91	+34:26:01.9	20.352	–	2.240
14	05:28:39.38	+34:24:33.2	18.892	–	1.980
15	05:28:39.85	+34:24:39.3	19.423	–	1.848
16	05:28:46.04	+34:24:07.5	21.147	–	2.419
17	05:28:48.08	+34:24:09.6	17.777	–	1.423
18	05:28:46.68	+34:22:18.9	19.751	–	1.828
19	05:28:49.55	+34:23:26.8	17.658	–	2.248
20	05:28:53.23	+34:23:35.2	19.581	–	2.587
21	05:28:56.05	+34:23:00.3	16.876	–	1.955
22	05:28:58.48	+34:23:10.2	18.579	–	2.439
23	05:29:03.31	+34:24:13.6	19.792	–	2.576
24	05:29:09.69	+34:23:32.2	18.000	–	2.287
25	05:29:19.14	+34:17:47.1	–		–

Point Source Catalogue (PSC) (Cutri et al. 2003). To improve the photometric accuracy, we used photometric quality flag (ph_qual = AAA) which gives an S/N $\geqslant$ 10 and a photometric uncertainty <0.10 mag. This selection criterion ensures best quality detection in terms of photometry and astrometry (cf. Lee et al. 2005). The *JHK*$_s$ data were transformed from 2MASS system to the California Institute of Technology (CIT) system using the relations given on the 2MASS web site.[2]

The *Midcourse Space Experiment* (*MSX*) surveyed the Galactic plane in four mid-infrared (MIR) bands – *A* (8.28 μm), *C* (12.13 μm), *D* (14.65 μm) and *E* (21.34 μm) at a spatial resolution of ∼18 arcsec (Price et al. 2001). Two of these bands (*A* and *C*) with λ(Δλ) corresponding to 8.28 μm (3.36 μm) and 12.13 μm (1.71 μm) include several polycyclic aromatic hydrocarbons (PAHs) features at 6.2, 7.7, 8.7, 11.3 and 12.7 μm. *MSX* images in these four bands around the cluster region were used to study the emission from the PAHs.

The data from the *IRAS* survey around the cluster region in the four bands (12, 25, 60, 100 μm) were HIRES processed (Aumann, Fowler & Melnyk 1990) to obtain high angular resolution maps. These maps were used to study the spatial distribution of dust colour temperature and optical depth.

4 RADIAL STELLAR SURFACE DENSITY AND CLUSTER SIZE

The radius of a cluster is one of the important parameters used to study the dynamical state of the cluster. We used star count technique to determine the statistical properties of clusters with respect to the surrounding stellar background, to study the surface density

---

[2] http://www.astro.caltech.edu/~jmc/2mass/v3/transformations/.

distribution of stars in the cluster region and to derive the radius of the cluster.

To determine the cluster centre, we used the stellar density distribution of stars having $V \leqslant 18$ mag in a ±75 pixel wide strip along both *X* and *Y* directions around an eye-estimated centre. The point of maximum density obtained by fitting a Gaussian curve is considered as the centre of the cluster. The coordinates of the cluster centre are found to be $\alpha_{2000} = 05^h28^m07\overset{s}{.}5 \pm 1\overset{s}{.}0$; $\delta_{2000} = +34°25'42'' \pm 15''$. The 2MASS NIR data yields the cluster centre ∼7 arcsec away southwards of the optical centre. However, this difference is within the uncertainty and therefore can be considered identical. Henceforth, we have used the optical centre as the centre of the cluster.

To investigate the radial structure of the cluster, we derived the radial density profile (RDP) using the Kiso Schmidt observations for stars brighter than $V = 18$ mag by dividing star counts inside the concentric annuli of 1 arcmin wide around the cluster centre by the respective annulus area. The densities thus obtained are plotted as a function of radius in Fig. 4, where 1 arcmin at the distance of cluster (2.05 kpc, cf. Section 6) corresponds to ∼0.6 pc. The upper and the lower panels show the RDPs obtained from optical and 2MASS NIR data, respectively. The error bars are derived assuming that the number of stars in each annulus follows Poisson statistics.

The radius of the cluster (r_{cl}) is defined as the point where the cluster stellar density merges with the field stellar density. The contribution of the field stars has been estimated by counting stars in the annular region 16–21 arcmin from the cluster centre. The horizontal dashed line in Fig. 4 shows the field star density. Optical RDP indicates a dip in stellar counts at $r \sim 6.5$ arcmin, whereas this dip is absent in NIR RDP. The NIR RDP indicates an enhancement in stellar density at $r \sim 7.5$ arcmin. To find out the cause of dip in the optical RDP and enhancement in stellar density in the NIR RDP, in Fig. 4, we also show RDPs for the eastern and western regions of Stock 8. The dip in the optical and enhancement in NIR RDP is visible only towards the western region of the cluster. A comparison of the RDPs with spatial distribution of $E(B − V)$, shown in Fig. 7, indicates that the dip in the optical RDP at $r \sim 6.5$ arcmin may be an artefact of relatively higher extinction around $r \sim 6.5$–7 arcmin. The NIR observations can probe deeper in the embedded region, hence enhancement in stellar density in NIR RDP around $r \sim$ 7.5 arcmin may be due to embedded population. Since star formation activity in the Nebulous Stream, as discussed in Section 11, is found to be independent of the star formation activity in the cluster region, we used radius of the cluster as $r_{cl} \sim 6$ arcmin (as obtained from optical data) to study the properties of the cluster.

To parametrize the RDP, we fitted the observed RDP with the empirical model of King (1962) which is given by

$$\rho(r) = \frac{f_0}{1 + (r/r_c)^2}, \tag{1}$$

where r_c is the core radius at which surface density $\rho(r)$ becomes half of the central density, f_0. The best fit to the observed RDPs, obtained by a χ^2 minimization technique, is shown in Fig. 4. The core radii thus estimated from optical and NIR RDPs are 1.4 ± 0.2 and 1.6 ± 0.1 arcmin, respectively.

5 REDDENING IN THE CLUSTER

The extinction in a star cluster arises due to two distinct sources: (1) the general ISM in the foreground of the cluster [$E(B − V)_{min}$] and (2) the localized cloud associated with the cluster [$E(B − V) = E(B − V)_* − E(B − V)_{min}$], where $E(B − V)_*$ is the reddening of the star embedded in the parent cloud. The former component
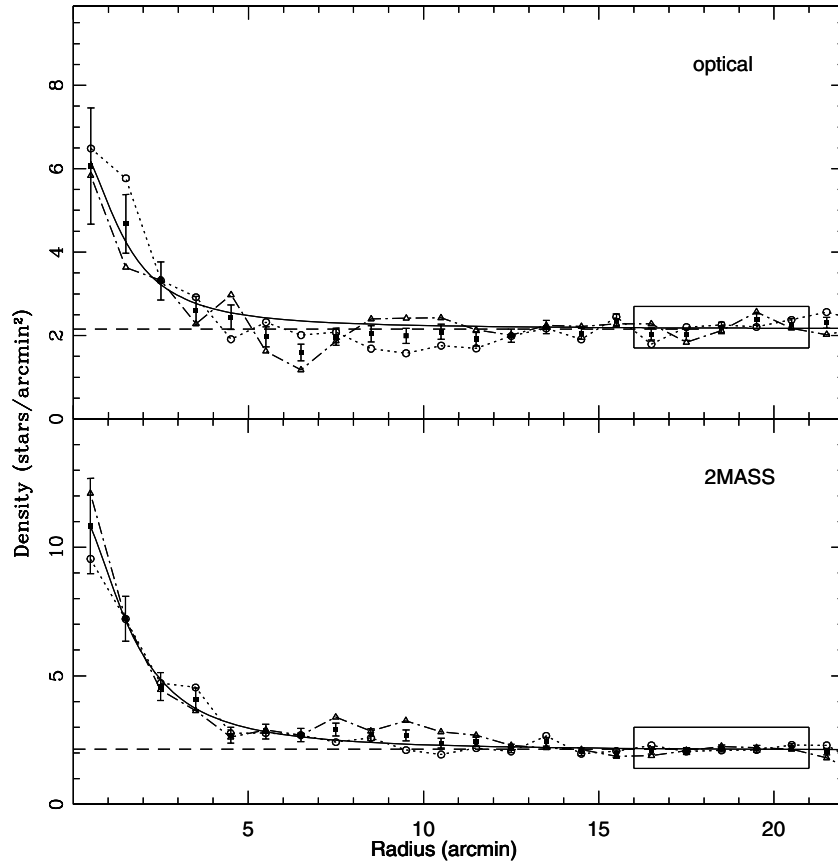
Figure 4. Stellar density (filled squares with error bars) as a function of radius from the adopted cluster centre for the optical and 2MASS data. The dashed line represents the mean density level of the field stars and the continuous curve shows the least-squares fit of the King (1962) profile to the observed data points from Kiso Schmidt observations. Open circles connected by dotted line and open triangles connected by dot–dashed line represent RDPs for the east and west region of the cluster, respectively. The error bars represent $\pm\sqrt{N}$ errors. Box represents the radial range considered as a field region.

is characterized by the ratio of the total-to-selective extinction R_V [$=A_V/E(B-V)$]$= 3.1$ (Wegner 1993; He et al. 1995; Winkler 1997), whereas for the intracluster regions of young clusters embedded in dust and gas cloud the value of R_V may vary significantly (Chini & Wargau 1990; Tapia et al. 1991; Hillenbrand et al. 1993; Pandey, Ogura & Sekiguchi 2000).

The ratio of total-to-selective extinction R is an important quantity, which must be known to get the dereddened magnitudes of the stars. Consequently, the value of R affects the distance determination significantly. Several studies have already pointed out anomalous reddening law with high R values in the vicinity of SFRs (see e.g. Neckel & Chini 1981; Chini & Krugel 1983; Chini & Wargau 1990; Hillenbrand et al. 1993; Pandey et al. 2000; Samal et al. 2007). Since the cluster is embedded in the parent molecular cloud, it will be useful to understand the reddening law in and around the Stock 8 region.

To study the nature of the extinction law in the cluster region, we used two-colour diagrams (TCDs) as described by Pandey et al. (2003). The TCDs of the form of $(V-\lambda)$ versus $(B-V)$, where λ is one of the broad-band filters (R, I, J, H, K, L), provide an effective method for separating the influence of the normal extinction produced by the diffuse interstellar medium from that of the abnormal extinction arising within regions having a peculiar distribution of dust sizes (cf. Chini & Wargau 1990; Pandey et al. 2000).

The TCDs for the region $r < 12$ arcmin are shown in Fig. 5. The $E(V-\lambda)/[E(B-V)]$ values in the cluster region are estimated

using the procedure as described in Pandey et al. (2003). The slopes of the distributions m_{cluster} (cf. Pandey et al. 2003) are found to be $1.13 \pm 0.01, 1.95 \pm 0.03, 2.41 \pm 0.03, 2.56 \pm 0.03$ for $(V-I)$, $(V-J), (V-H), (V-K)$ versus $(B-V)$ diagrams, respectively. Identical values for the slopes are found for the region $r < 6$ arcmin. The ratio of total-to-selective extinction in the cluster region, R_{cluster}, is also derived using the procedure given by Pandey et al. (2003). The ratios $E(V-\lambda)/[E(B-V)\,(\lambda \geqslant \lambda_I)]$ yield $R_{\text{cluster}} = 3.1 \pm 0.1$ which indicates a normal reddening law in the cluster region.

In the absence of spectroscopic observations, the interstellar extinction $E(B-V)$ towards the cluster region can be estimated using the $(U-B)/(B-V)$ colour–colour (CC) diagram. The CC diagram of the cluster region ($r \leqslant 6$ arcmin) is presented in Fig. 6. Since the cluster is very young, a variable reddening is expected within the cluster region. The figure also indicates a large amount of contamination due to field stars. The probable foreground stars follow the intrinsic zero-age main-sequence (ZAMS) by Girardi et al. (2002) reddened by $E(B-V) = 0.20$ mag along a normal reddening vector [i.e. $E(U-B)/E(B-V) = 0.72$]. In Fig. 6, the continuous line represents the theoretical ZAMS which is shifted by $E(B-V) = 0.40$ and 0.60 mag, respectively, along the normal reddening vector to match the observations of probable cluster members. Fig. 6 yields a variable reddening with $E(B-V)_{\text{min}} = 0.40$ mag to $E(B-V)_{\text{max}} = 0.60$ mag in the cluster region. A careful inspection of CC diagram indicates the presence of further reddened population. The theoretical ZAMS, shown by dot–dashed line, is further shifted to
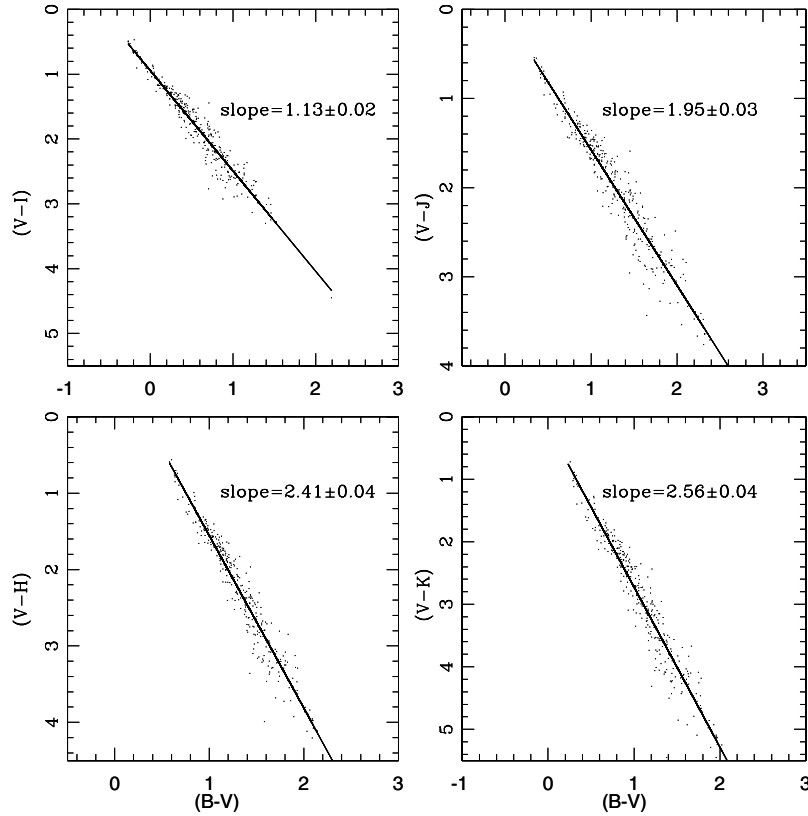
Figure 5. TCDs for stars within the radius $r \leqslant 12$ arcmin from the centre of Stock 8. The continuous line represents the least-squares fit to the data.
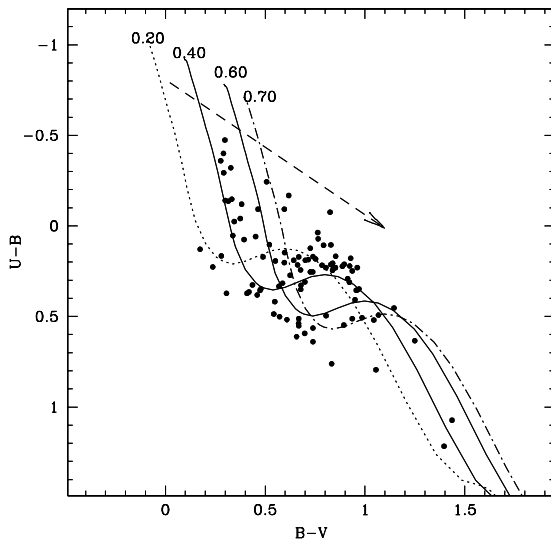
Figure 6. $(U - B)/(B - V)$ CC diagram for the stars within the region $r \leqslant 6$ arcmin. The dotted curve represents the ZAMS by Girardi et al. (2002) shifted along the reddening slope of 0.72 (shown as a dashed line) for $E(B - V) = 0.20$ mag (probable foreground stars). The continuous curves are the ZAMS shifted by $E(B - V) = 0.40$ and 0.60 mag, respectively, to match the observations of probable cluster members. The dot–dashed curve represents the ZAMS reddened by $E(B - V) = 0.70$ mag to match the probable background population (see text).

match the reddened sequence. This population may belong to blue plume (BP) of Norma–Cygnus arm (cf. Carraro et al. 2005; Pandey, Sharma & Ogura 2006). The $E(B - V)$ value for the background population comes out to be ~ 0.70 mag, which is comparable to the

$E(B - V)$ value of BP population around $l \sim 170°$ (cf. Pandey et al. 2006).

Reddening of individual stars having spectral types earlier than A0 have also been computed by means of the reddening free index Q (Johnson & Morgan 1953). Assuming a normal reddening law we can construct a reddening-free parameter index $Q = (U - B) - 0.72\ (B - V)$. For the MS stars, the intrinsic $(B - V)_0$ colour and colour-excess can be obtained from the relation $(B - V)_0 = 0.332\ Q$ (Johnson 1966; Hillenbrand et al. 1993) and $E(B - V) = (B - V) - (B - V)_0$, respectively. The distribution of reddening as a function of radial distance from the cluster centre is shown in Fig. 7, which indicates a slight enhancement of $E(B - V)$ at $r \sim 7$ arcmin. In Fig. 7 we also show variation of reddening towards eastern and western directions of the cluster. From the figure it can be noted that the reddening towards eastern region of the cluster is rather uniform whereas the reddening towards the western region of the cluster shows relatively higher value (although statistically weak) at $r \sim 7$ arcmin.

6 OPTICAL COLOUR–MAGNITUDE DIAGRAMS

The optical colour–magnitude diagrams (CMDs) were used to derive the cluster fundamental parameters such as age, distance, etc. The $V/(B - V)$ and $V/(V - I)$ CMDs of stars within radial distance $r \leqslant 6$ arcmin of Stock 8 and $V/(V - I)$ CMD for the nearby field region are shown in Fig. 8. The contamination due to background field population is apparent in the CMDs of the cluster region. The CMDs of the cluster region also show a significant number of stars towards the right-hand side of the ZAMS. Stars brighter than
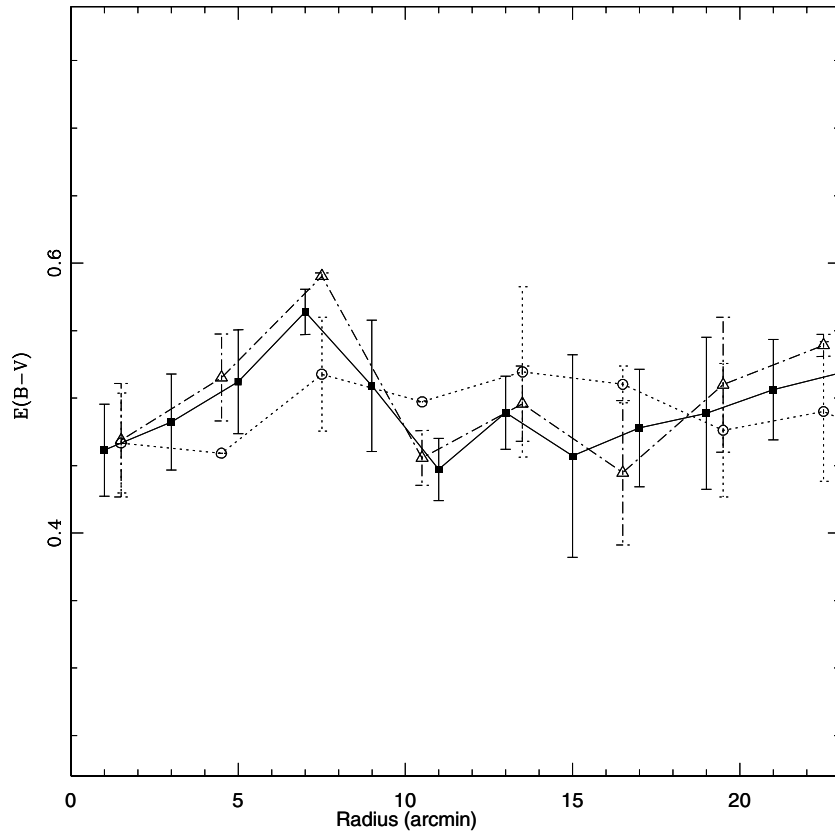
Figure 7. Distribution of average reddening (filled squares) as a function of radial distance from the cluster centre. Error bars represent standard errors. Open circles connected by dotted line and open triangles connected by dot–dashed line represent distribution of average reddening in the east and west region of the cluster, respectively.
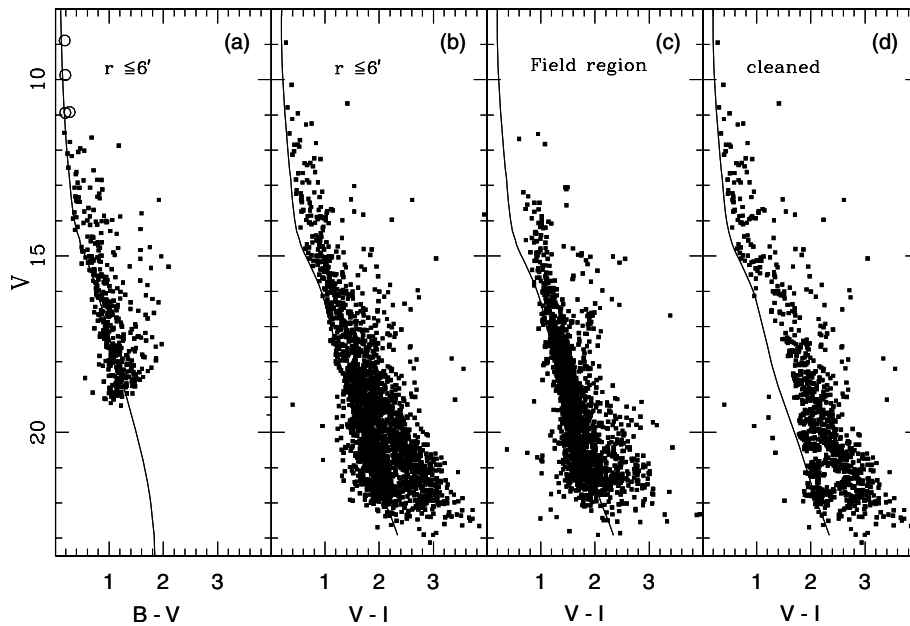

Figure 8. (a and b) *V/(B − V)* and *V/(V − I)* CMDs for stars within the region *r* ⩽ 6 arcmin of the cluster Stock 8; (c) *V/(V − I)* CMD for stars in the nearby field region having same area as in panels (a) and (b); (d) statistically cleaned *V/(V − I)* CMD for the cluster region. The continuous line is the isochrone of 2 Myr from Girardi et al. (2002) corrected for the cluster distance and reddening. The stars in *V/(B − V)* CMD shown by open circles are taken from Mayer & Macak (1971).

$V \sim 11.5$ mag observed in *B* band using Kiso Schmidt telescope are saturated even in frames with short exposure.

To study the LF/MF, it is necessary to remove field star contamination from the sample of stars in the cluster region. Membership determination is also crucial for assessing the presence of PMS stars because both PMS and dwarf foreground stars occupy similar positions above the ZAMS in the CMDs. In the absence of proper-motion study, we used statistical criterion to estimate the number of probable member stars in the cluster region. To remove contamination of field stars from the MS and PMS sample, we statistically subtracted the contribution of field stars from the observed CMD of the cluster region using the following procedure. For any star in the $V/(V - I)$ CMD of the field region, the nearest star in the cluster's $V/(V - I)$ CMD within $V \pm 0.125$ and $(V - I) \pm 0.065$ of the field star was removed. While removing stars from the cluster CMD, necessary corrections for incompleteness of the data sample were taken into account. The statistically cleaned $V/(V - I)$ CMD of the cluster region is shown in Fig. 8(d) which clearly shows a sequence towards red side of the MS. The contamination due to field stars at $V > 20$ mag and $(V - I) \sim 2.1$ mag can still be seen in Fig. 8(d).

In Fig. 8, using $E(B - V)_{min} = 0.40$ mag and relations $A_V = 3.1 E(B - V)$, $E(V - I) = 1.25 E(B - V)$, we visually fitted theoretical isochrone of log age = 6.3 (2 Myr) and $Z = 0.02$ by Girardi et al. (2002) to the blue envelope of the observed MS. We estimated a distance modulus of $(m - M)_V = 12.8 \pm 0.15$ mag which corresponds to a distance of 2.05 ± 0.10 kpc. Fig. 9 shows dereddened $V_0/(B - V)_0$ CMD of the stars lying within $r \leqslant 6$ arcmin. The stars having spectral type earlier than A0 were dereddened individually using the Q method as discussed in Section 5. Because bright stars in our observations got saturated even in short exposure frames, we obtained their *B*-band data from Mayer & Macak (1971). The isochrone for 2 Myr by Girardi et al. (2002) are also plotted in the figure. This figure yields an average post-main-sequence age of the massive stars of the cluster as $\leqslant 2$ Myr.
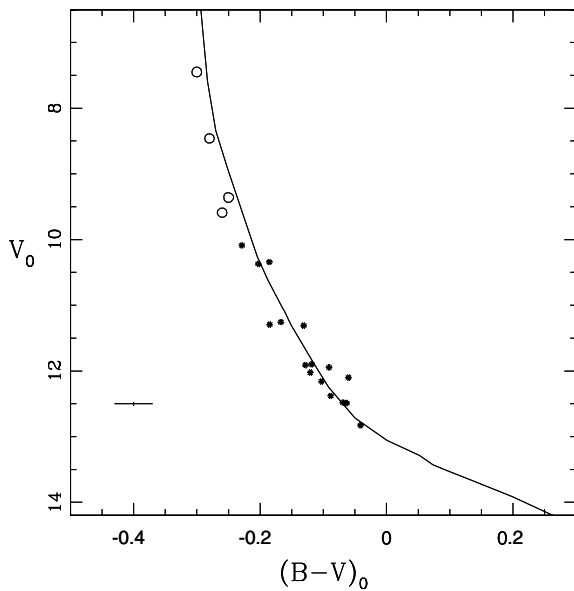
Figure 9. $V_0/(B - V)_0$ CMD for stars lying within the region $r \leqslant 6$ arcmin of the cluster Stock 8. The data for stars shown by open circles are taken from Mayer & Macak (1971). The isochrone (continuous curve) for 2 Myr by Girardi et al. (2002) is also shown. The average photometric errors in magnitude and colour are shown in the lower left-hand side of the figure.

In Fig. 10 we have plotted $V/(V - I)$ CMD for the young stellar objects (YSOs), i.e. Hα emission and NIR-excess sources (cf. Section 7.1) lying within regions $r \leqslant 6$ arcmin and $6 < r \leqslant 12$ arcmin. The Hα sources are represented by open and filled triangles and the NIR-excess sources by open and filled circles. The PMS isochrones by Siess, Dufour & Forestini (2000) for 0.5, 5, 10 Myr (dashed lines) and isochrone for 2 Myr by Girardi et al. 2002 (continuous line) are also shown. Fig. 10 reveals that majority of the YSOs (i.e. Hα and NIR-excess stars) have ages $\leqslant$5Myr. The age spread may indicate a non-coeval star formation in the cluster. Fig. 10 also indicates a tendency that stars lying at $r > 6$ arcmin are relatively younger than those in the cluster region.

In Fig. 11 we have shown statistically cleaned CMD along with PMS isochrones for ages 0.5 and 10 Myr by Siess et al. (2000). The 2-Myr isochrone by Girardi et al. (2002) and evolutionary tracks by Siess et al. (2000) for different masses are also shown. A comparison of Fig. 10 with Fig. 11 suggests that the stars lying on the right-hand side of the MS in Fig. 11 may be probable PMS stars. The stars lying between the 0.5–10 Myr isochrones are considered as PMS stars and this set of data is used for calculation of the IMF (see Section 8).

7 NEAR-INFRARED COLOUR–COLOUR AND COLOUR–MAGNITUDE DIAGRAMS

The NIR data are very useful to study the nature of young stellar population within the SFRs. From 2MASS PSC, we obtained JHK_s data (with photometric errors $\leqslant 0.1$ mag in all the three bands) for 445 and 898 NIR sources lying within $r \leqslant 6$ arcmin and $6 < r \leqslant 12$ arcmin, respectively. In the following Section, we discuss NIR CC diagram and CMDs.

7.1 Colour–colour diagram

The $(J - H)/(H - K)$ CC diagrams for the cluster region $r \leqslant 6$ arcmin, outside the cluster region $6 < r \leqslant 12$ arcmin, and a nearby field region are shown in Fig. 12. The thin and thick solid lines are the locations of unreddened main-sequence and giant stars (Bessell & Brett 1988), respectively. The dotted line represents the locus of T Tauri stars (Meyer, Calvet & Hillenbrand 1997). The parallel dashed lines are the reddening vectors for the early MS and giant type stars (drawn from the base and tip of the two branches). The crosses on the dashed lines are separated by an A_V value of 5 mag. The extinction ratios, $A_J/A_V = 0.265, A_H/A_V = 0.155$ and $A_K/A_V = 0.090$, are adopted from Cohen et al. (1981). All the 2MASS magnitudes and colours have been converted into the CIT system. The curves are also in the CIT system.

Presently YSOs are classified as an evolutionary sequence spanning a few million years as: Class 0/Class I – the youngest embedded protostars surrounded by infalling envelopes and growing accretion disc; Class II – PMS stars with less active accretion discs and Class III – PMS stars with no discs or optically thin remnant dust (Adams, Lada & Shu 1987). Following Ojha et al. (2004a), we classified sources according to their locations in $(J - H)/(H - K)$ CC diagrams. The 'F' sources are those located between the reddening vectors projected from the intrinsic colour of main sequence and giant. These are considered to be field stars (main-sequence, giants) or Class III /Class II sources with small NIR excesses. The 'T' sources are located redward of 'F' but blueward of the reddening line projected from the red end of the T Tauri locus of Meyer et al. (1997). These sources are considered to be mostly classical T Tauri stars (Class II objects) with large NIR excesses. There may be an overlap in NIR colours of Herbig Ae/Be stars and T Tauri stars in
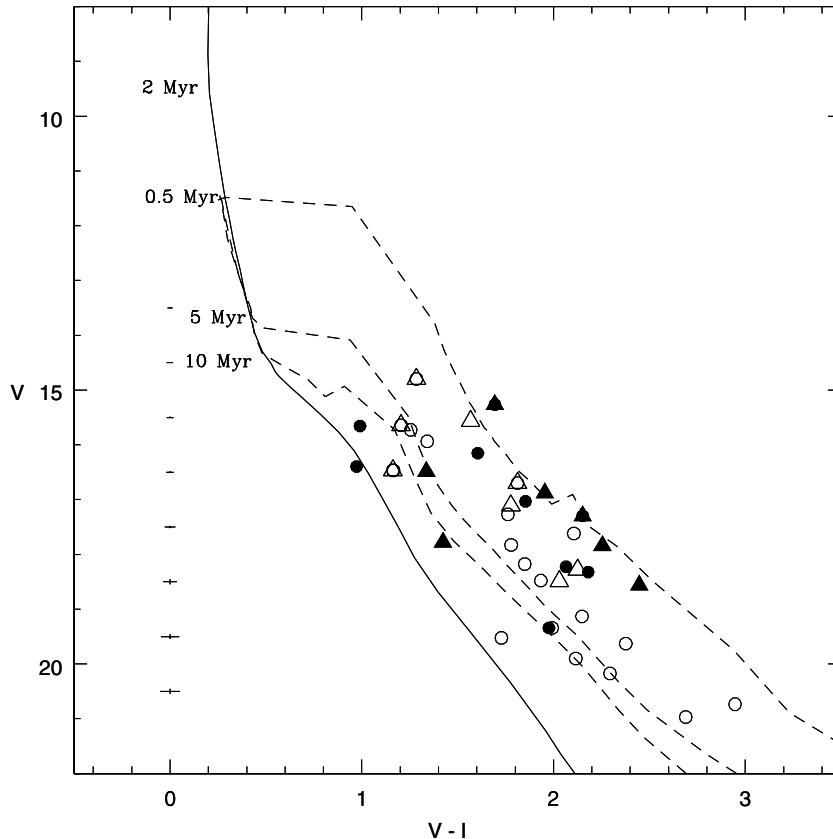
Figure 10. The $V/(V - I)$ CMD for Hα emission (open and filled triangles) and NIR-excess stars (open and filled circles), lying within the regions $r \leqslant 6$ arcmin and $6 < r \leqslant 12$ arcmin, respectively. Isochrone for 2 Myr by Girardi et al. (2002) (continuous curve) and PMS isochrones for 0.5, 5, 10 Myr by Siess et al. (2000) (dashed curves) are also shown. All the isochrones are corrected for the distance of 2.05 kpc and reddening $E(B - V) = 0.40$ mag. Average photometric errors in $(V - I)$ colour as a function of magnitudes are shown in the left-hand side of the figure.

the 'T' region (Hillenbrand et al. 1992). The 'P' sources are those located in the region redward of region 'T' and are most likely Class I objects (protostellar objects).

In Fig. 12, a significant number of stars show NIR excess indicating that the Stock 8 region is populated by YSOs. A comparison of the CC diagrams of the cluster region with the field region (Fig. 12c) indicates that stars in the cluster region having $J - H > 0.6$ and lying towards the right-hand side of the reddening vector at the boundary of 'F' and 'T' regions can be safely considered as NIR-excess stars. This criterion yields 19 and 17 NIR-excess sources in the Stock 8 ($r \leqslant 6$ arcmin) and outside the cluster ($6 < r \leqslant 12$ arcmin) regions, respectively, which are shown as open and filled circles in Fig. 12. Distribution of Hα emission stars is also shown as open ($r \leqslant 6$ arcmin) and filled ($6 < r \leqslant 12$ arcmin) triangles. Fig. 12 indicates that the YSOs located outside the cluster region have relatively higher extinction and NIR excess as compared to those located in the inner region. The distribution of NIR excess, $\Delta(H - K)$, defined as horizontal displacement from the reddening vector at the boundary of 'F' and 'T' regions (cf. Fig. 12), for the two regions is shown in Fig. 13 which manifests that YSOs located in the region $6 < r \leqslant 12$ arcmin have relatively higher NIR excess.

7.2 Colour–magnitude diagrams

The $K/(H - K)$ and $J/(J - H)$ CMDs for the NIR-excess and Hα sources detected within $r \leqslant 12$ arcmin region are shown in Figs 14

and 15. The isochrone for age 2 Myr by Girardi et al. (2002) and PMS isochrones for ages 0.5, 10 Myr by Siess et al. (2000), respectively, have been plotted assuming a distance of 2.05 kpc and an extinction of $E(B - V)_{min} = 0.40$ mag as obtained from the optical data. Fig. 14 also indicates that sources lying outside the cluster region, i.e. $6 < r \leqslant 12$ arcmin have relatively higher NIR excess. Therefore, from Figs 10, 12–14, we infer that sources lying in the region $6 < r \leqslant 12$ arcmin may possibly be younger than those located in the cluster region ($r \leqslant 6$ arcmin).

The mass of the probable YSO candidates can be estimated by comparing their locations on the CMD with the evolutionary models of PMS stars. To estimate the stellar masses, the J luminosity is recommended rather than that of H or K, as the J band is less affected by the emission from circumstellar material (Bertout, Basri & Bouvier 1988). In Fig. 15, the continuous oblique reddening lines denote the positions of PMS stars of 0.5 Myr age having masses 0.1, 1.0 and 3.0 M$_\odot$. The YSOs, in general, have masses in the range 0.1–3.0 M$_\odot$.

8 INITIAL MASS FUNCTION

Young clusters are important tools to study the IMF since their MF can be considered as the IMF as they are too young to lose significant number of members either by dynamical or stellar evolution. To study the IMF of Stock 8 we used the data within $r \leqslant 6$ arcmin.
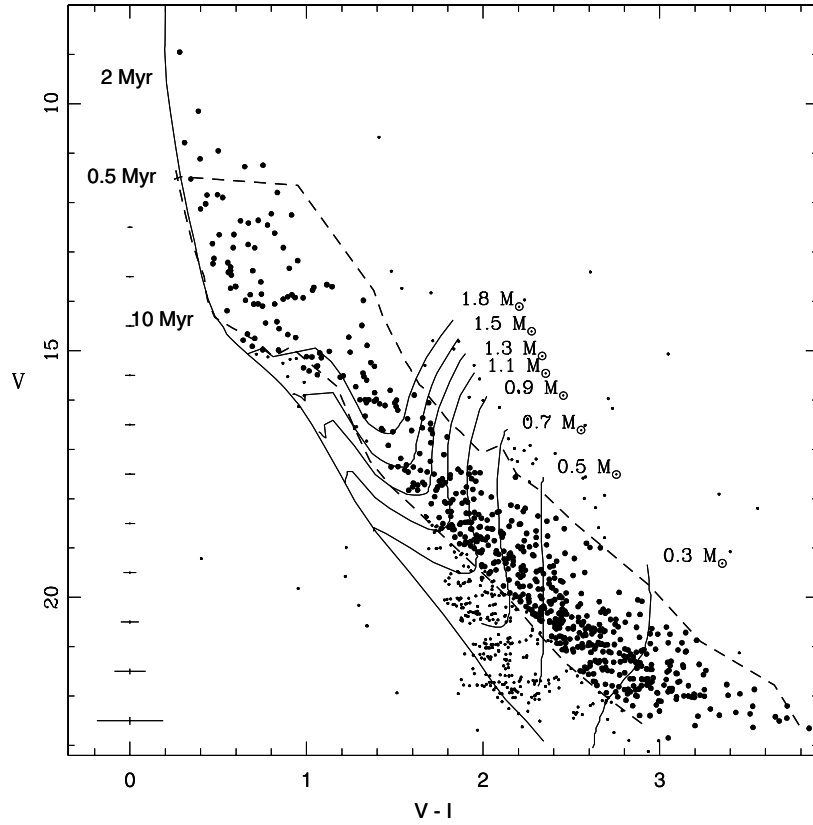
Figure 11. Statistically cleaned $V/(V − I)$ CMD for stars lying within the region $r \leqslant 6$ arcmin of Stock 8 and between PMS isochrones of age 0.5 and 10 Myr. The isochrone for 2 Myr age by Girardi et al. (2002) and PMS isochrones of 0.5, 10 Myr along with evolutionary tracks of different mass stars by Siess et al. (2000) are also shown. All the isochrones are corrected for the cluster distance and reddening. The corresponding values of masses in solar mass are given at the right-hand side of each track. Points shown by small dots are considered as non-members. Average photometric errors in $(V − I)$ colour as a function of magnitudes are shown in the left-hand side of the figure.
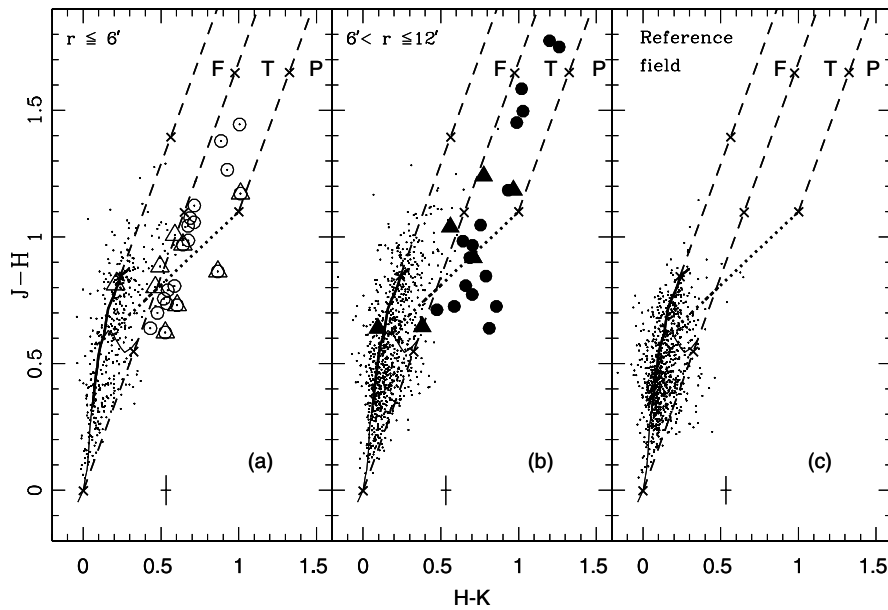
Figure 12. $(J − H)/(H − K)$ CC diagrams of sources detected in the JHK_s bands with photometric errors less than 0.1 mag in (a) Stock 8 region ($r \leqslant 6$ arcmin); (b) outside the Stock 8 region $6 < r \leqslant 12$ arcmin; (c) the nearby reference field. The locus for dwarfs (thin solid curve) and giants (thick solid curve) are from Bessell & Brett (1988). The dotted line represents the locus of T Tauri stars (Meyer et al. 1997). Dashed straight lines represent the reddening vectors (Cohen et al. 1981). The crosses on the dashed lines are separated by $A_V = 5$ mag. The open and filled triangles are Hα emission sources while open and filled circles are NIR-excess sources for the inner and outer regions, respectively. The average photometric errors are shown in the lower left-hand part of the panels.
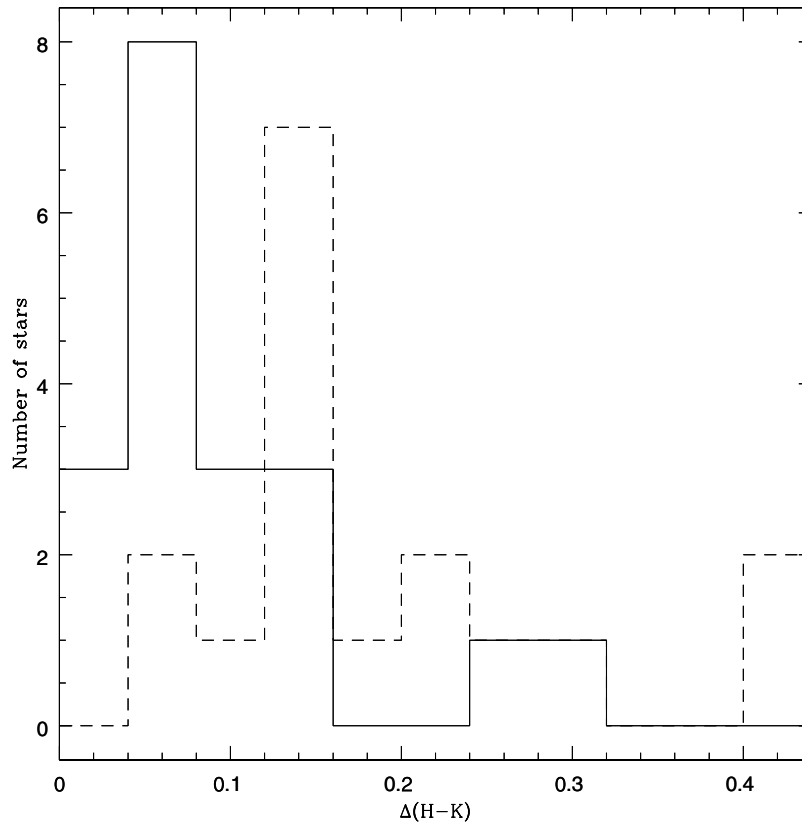
Figure 13. Distribution of NIR excess in two regions. Continuous and dashed line histograms show the distribution in $r \leqslant 6$ arcmin and $6 < r \leqslant 12$ arcmin regions, respectively.
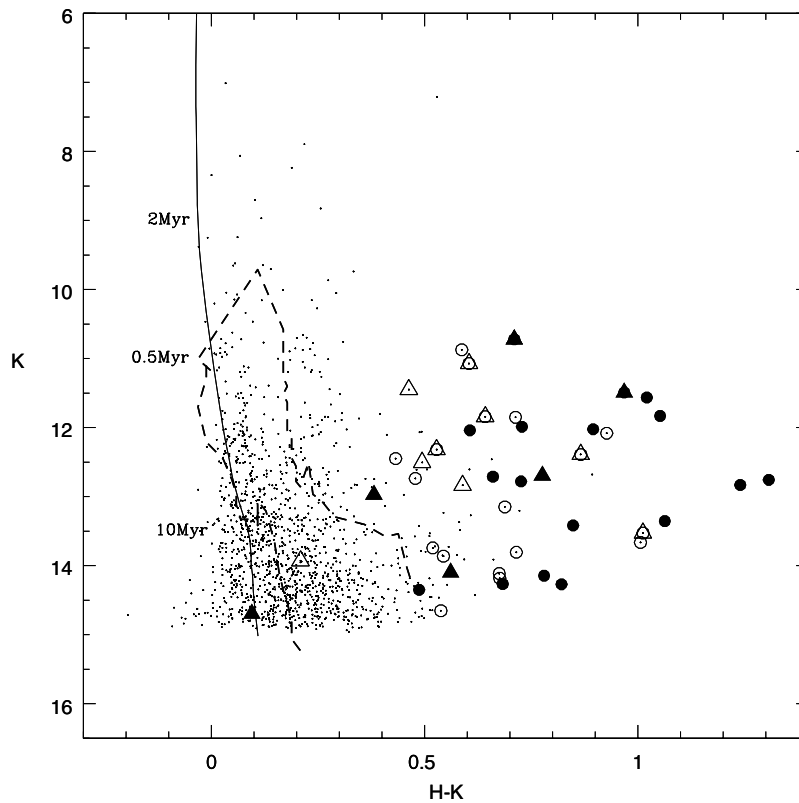
Figure 14. $K/(H - K)$ CMD for stars within the region $r \leqslant 12$ arcmin. The symbols are same as in Fig. 10. Isochrone for 2 Myr by Girardi et al. (2002) (continuous curve) and PMS isochrones from 0.5 and 10 Myr by Siess et al. (2000) (dashed curves), corrected for cluster distance and reddening are also shown.
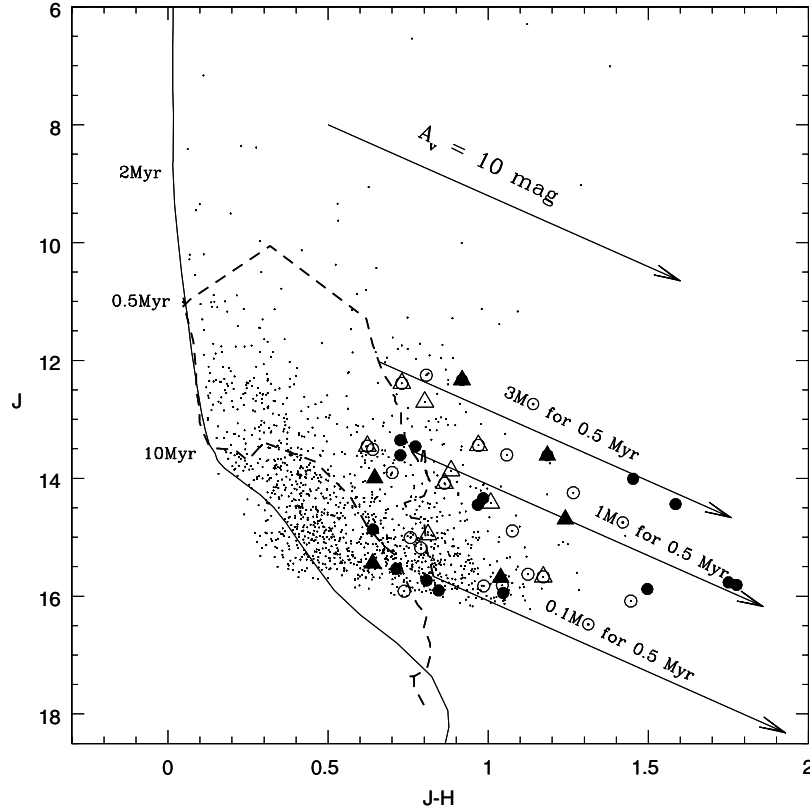
Figure 15. $J/(J - H)$ CMD for stars within the region $r \leqslant 12$ arcmin. The symbols are same as in Fig. 10. The isochrone of 2 Myr (continuous curve) by Girardi et al. (2002) and PMS isochrones of age 0.5 and 10 Myr (dashed curves) by Siess et al. (2000), corrected for cluster distance and reddening are also shown. The continuous oblique reddening lines denote the positions of PMS stars of 0.1, 1.0 and 3.0 $M_{\odot}$ for 0.5 Myr.

The MF is often expressed by the power law, $N(\log m) \propto m^{\Gamma}$, and the slope of the MF is given as

$$\Gamma = \mathrm{d} \log N(\log m)/\mathrm{d} \log m,$$

where $N(\log m)$ is the number of stars per unit logarithmic mass interval. For the mass range $0.4 < M/M_{\odot} \leqslant 10$, the classical value derived by Salpeter (1955) for the slope of IMF is $\Gamma = -1.35$.

With the help of statistically cleaned CMD shown in Fig. 11, we can derive the MF using theoretical evolutionary models. Since the post-main-sequence age of the cluster is $\leqslant 2$ Myr, stars having $V \leqslant 15$ mag have been considered to be on the main sequence. For the MS stars LF was converted to MF using the theoretical model by Girardi et al. (2002) (cf. Pandey et al. 2000, 2001). The MF for PMS stars was obtained by counting the number of stars in various mass bins (shown as evolutionary tracks in Fig. 11). Necessary corrections for incompleteness of the data sample were taken into account for each magnitude bin to calculate the MF. The MF of the cluster is plotted in Fig. 16. The slope of the MF Γ, in the mass range $1.0 \leqslant M/M_{\odot} < 13.4$, can be represented by a power law having a slope of $\Gamma = -1.38 \pm 0.12$, which agrees well with Salpeter value (-1.35). In the mass range $0.3 \leqslant M/M_{\odot} < 1.0$, the MF also follows a power law but with a shallower slope $\Gamma = -0.58 \pm 0.23$ indicating a break in the slope of the MF at $\sim 1 \, M_{\odot}$. The break in the power law has already been reported in the case of a few young clusters, e.g. Trapezium and IC 348 (Muench et al. 2002, 2003). They showed a flattening in slope of the IMF at $\sim 0.6 \, M_{\odot}$. Recently, in the case of young clusters NGC 1893 (Sharma et al. 2007) and Be 59 (Pandey et al. 2007), a break in the power law was reported at ~ 2 and $2.5 \, M_{\odot}$, respectively. However, $\Gamma = -0.58 \pm 0.23$ obtained for

Stock 8 below $1 \, M_{\odot}$ is shallower than that obtained for NGC 1893 (-0.88 ± 0.09) and is steeper than that obtained for Be 59 (approximately flat). In the case of NGC 2362 the MF flattens at ~ 3–$1 \, M_{\odot}$ (Damiani et al. 2006) which is at a much higher mass than observed in some young clusters. Prisinzano et al. (2005) found that the MF of young open cluster NGC 6530, in the mass range $0.4 \leqslant M/M_{\odot} < 4.0$, can be represented by a power law having slope (-1.22 ± 0.17). However, the MF does not flatten below $\sim 0.6 \, M_{\odot}$ as in the case of some young clusters, e.g. Trapezium, Taurus and IC 348, instead it decreases for masses lower than $\sim 0.4 \, M_{\odot}$. Here it is worthwhile to mention that exclusion of the lowest mass bin in Fig. 16 will yield a shallower slope $\Gamma = -0.3 \pm 0.3$, although with large error, for masses below $1 \, M_{\odot}$, which is comparable with the slope obtained by Muench et al. (2002, 2003) for Trapezium and IC 348 clusters. However, a deeper photometry is required to study the nature of MF of Stock 8 below $1 \, M_{\odot}$.

The mass segregation, in the sense that massive stars being more centrally concentrated than the lower mass stars, has been reported in several Large Magellanic Cloud (LMC) and Milky Way star clusters (see Pandey, Mahra & Sagar 1992; Fischer et al. 1998; Pandey et al. 2001; de Grijs et al. 2002a,b,c; Pandey et al. 2005; Chen, de Grijs & Zhao 2007). In the case of intermediate or old clusters, the mass segregation is mainly due to the effect of dynamical evolution. But in the case of young clusters the mass segregation may be the imprint of star formation process. To characterize the degree of mass segregation in Stock 8, we plotted cumulative distribution of stars as a function of distance from the cluster centre in two mass groups as shown in Fig. 17. The left-hand panel shows the distribution for mass groups $4 \leqslant M/M_{\odot} < 13.4$ (high-mass group) and
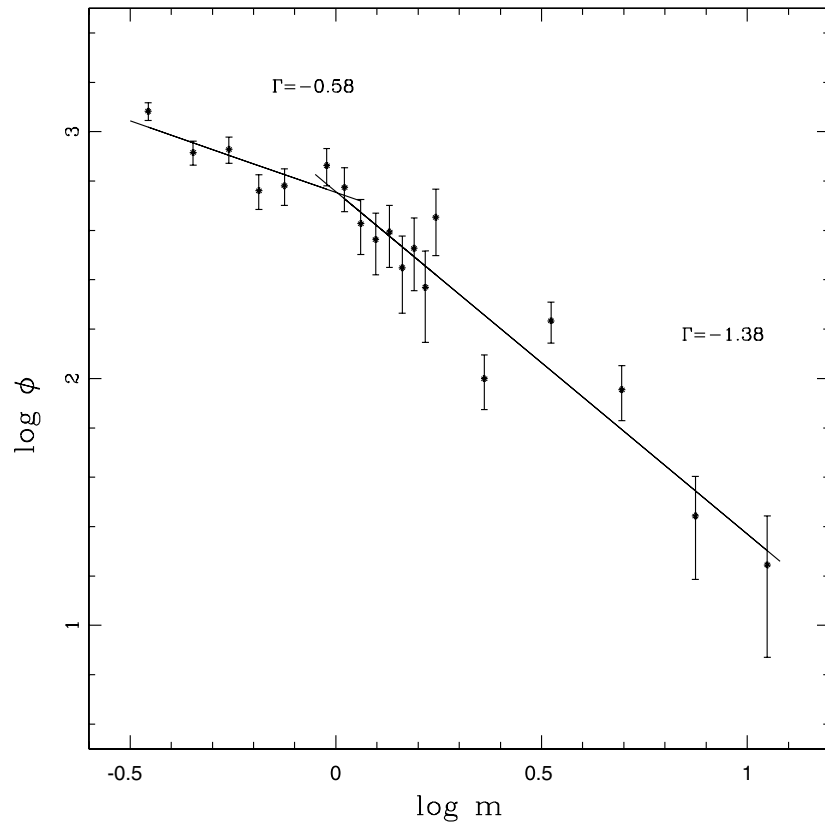
Figure 16. A plot of the MF for the cluster region $r \leqslant 6$ arcmin. The ϕ represents N/d log m. The error bars represent $\pm\sqrt{N}$ errors. The continuous lines show least-squares fit to the mass ranges described in the text. The values of the slopes obtained are also mentioned in the figure.
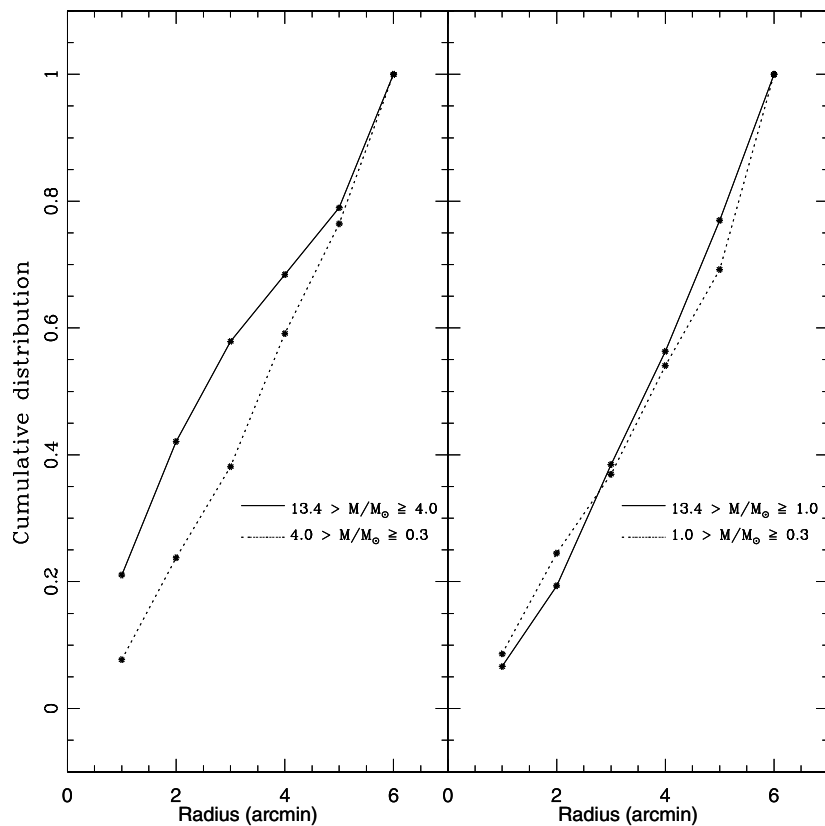
Figure 17. Cumulative distributions of stars of different mass intervals as a function of radial distance.

Table 5. CF of 2MASS data in the cluster and field regions.

K range (mag)	Stock 8 $r \leqslant 3$ arcmin	$3 < r \leqslant 6$ arcmin	Field region
10.0–10.5	1.00	1.00	1.00
10.5–11.0	1.00	1.00	1.00
11.0–11.5	1.00	1.00	0.98
11.5–12.0	1.00	1.00	0.97
12.0–12.5	0.95	0.96	0.91
12.5–13.0	0.99	1.00	0.96
13.0–13.5	0.94	0.94	0.97
13.5–14.0	0.96	0.96	0.97

$0.3 \leqslant M/M_\odot < 4$ (low-mass group), whereas the right-hand panel shows the distribution for $1.0 \leqslant M/M_\odot < 13.4$ (high-mass group) and $0.3 \leqslant M/M_\odot < 1.0$ (low-mass group). The Kolmogorov–Smirnov test indicates that the left-hand panel shows mass segregation at a confidence level of ∼75 per cent, whereas the right-hand panel does not show any mass segregation. This indicates that mass segregation, although weak, is effective only towards the higher mass end. Since variation of reddening within the cluster is not significant (cf. Fig. 7), and incompleteness of the data does not depend on the radial distance (cf. Table 3), we believe that the mass segregation may be the imprint of star formation process.

The *K*-band luminosity function (KLF) is a powerful tool to investigate the IMF of young embedded star clusters. During the last decade several studies have been carried out with the aim of determining the KLF of young open clusters (e.g. Lada & Lada 2003; Ojha et al. 2004b; Sanchawala et al. 2007). We have used 2MASS K_s-band data to study the KLF in Stock 8 region. The completeness of the 2MASS data is obtained by using ADDSTAR routine as discussed in Section 2.1. The CFs obtained for two subregions are given in Table 5. The KLF in Stock 8 region is studied by using the Besançon Galactic model of stellar population synthesis (Robin et al. 2003) and stars from a nearby reference field to take into account foreground/background field star contamination (cf. Sharma et al. 2007). The reference field, also taken from 2MASS, is located at a radial distance of ∼30 arcmin away from the cluster centre. Star counts are predicted using the Besançon model towards the direction of the control field. An advantage of using this model is that we can simulate foreground ($d < 2.05$ kpc) and the background ($d > 2.05$ kpc) field star populations separately. The foreground population was simulated using the model with $A_V = 1.24$ mag [$E(B - V) = 0.40$ mag] (cf. Section 5) and $d < 2.05$ kpc. The background population ($d > 2.05$ kpc) was simulated with $A_V = 1.86$ mag. Thus we determined the fraction of the contaminating stars (foreground + background) over the total model counts. This fraction was used to scale the nearby reference field and subsequently the star counts of the modified control field were subtracted from the KLF of the cluster to obtain the final corrected KLF. The scalefactor in different magnitude bins was found to be in the range of 0.8–1.0 with a mean value of ∼0.9.

The KLF is expressed by following power law:

$$\frac{dN(K)}{dK} \propto 10^{\alpha K},$$

where d$N(K)$/dK is the number of stars per 0.5-mag bin and α is the slope of the power law. The KLF for the cluster region $r \leqslant 6$ arcmin shown in Fig. 18, yields a slope of 0.31 ± 0.02, which is smaller than the average value of slopes ($\alpha \sim 0.4$) for young clusters (Lada et al. 1991; Lada & Lada 1995, 2003). Smaller values of KLF slope (∼0.3–0.2) have been reported for various young embedded clusters (Megeath et al. 1996; Chen, Tafalla & Greene 1997; Brandl, Brandner & Eisenhauer 1999; Ojha et al. 2004b; Leistra et al. 2005; Pandey et al. 2007; Sanchawala et al. 2007).

The KLF of Stock 8 is worth comparing with those of NGC 1893 and Be 59 since all the KLFs are obtained using a similar technique (NGC 1893, Sharma et al. 2007; Be59, Pandey et al. 2007). The slope ($\alpha = 0.31 \pm 0.02$) obtained for Stock 8 is in agreement with those obtained for NGC 1893 ($\alpha = 0.34 \pm 0.07$) and Be 59 ($\alpha = 0.27 \pm 0.02$).

9 EMBEDDED CLUSTER IN THE NEBULOUS STREAM

A Nebulous Stream, as identified in Fig. 1, is clearly seen towards the eastern region of the cluster, Stock 8. An embedded cluster, at a radial distance of ∼13 arcmin from the centre of Stock 8, can be noticed in the Nebulous Stream at $\alpha_{2000} = 05^h29^m00^s$; $\delta_{2000} = +34°23'12''$. Its 2MASS K_s-band image together with the distribution of NIR-excess stars and Hα emitters is shown in Fig. 19. Borissova et al. (2003) detected this cluster in their search for 2MASS PSC and designated it as CC 14. Recently, Ivanov et al. (2005) have studied CC 14 using deep NIR observations. They estimated a distance modulus $(m - M)_0 = 16.6 \pm 0.8$ mag, corresponding to a distance of

Table 6. List of OB stars in IC 417 region.

Star no.	α (2000) (h:m:s)	δ (2000) (° : ′ : ″)	Spectral type	$E(B - V)$ mag	References
1	05:28:07	+34:25:27	O9.5 V	–	Georgelin, Georgelin & Roux (1973)
			B0 IV	0.48	Mayer & Macak (1971)
2	05:27:35	+34:27:00	O8 V	1.25	Mayer & Macak (1971)
3	05:27:29	+34:25:03	O9 IV-V	0.98	Mayer & Macak (1971)
4	05:27:23	+34:23:41	B0 V	0.55	Mayer & Macak (1971)
5	05:28:08	+34:25:14	B1 V	0.46	Mayer & Macak (1971)
6	05:27:06	+34:19:32	B0.5 V	0.44	Mayer & Macak (1971)
7	05:27:16	+34:25:44	B0.5 V	0.45	Mayer & Macak (1971)
8	05:28:08	+34:23:45	B0.5 V	0.47	Mayer & Macak (1971)
9	05:28:06	+34:27:22	B1.5 V	0.52	Mayer & Macak (1971)
10	05:27:17	+34:30:57	B2 V	0.54	Mayer & Macak (1971)
11	05:27:43	+34:31:56	B0.5 IV	0.60	Savage (1985)
12	05:28:06	+34:25:00	B1 V	0.45	Mayer & Macak (1971)
13	05:28:39	+34:40:09	O8 V	0.57	Savage (1985)
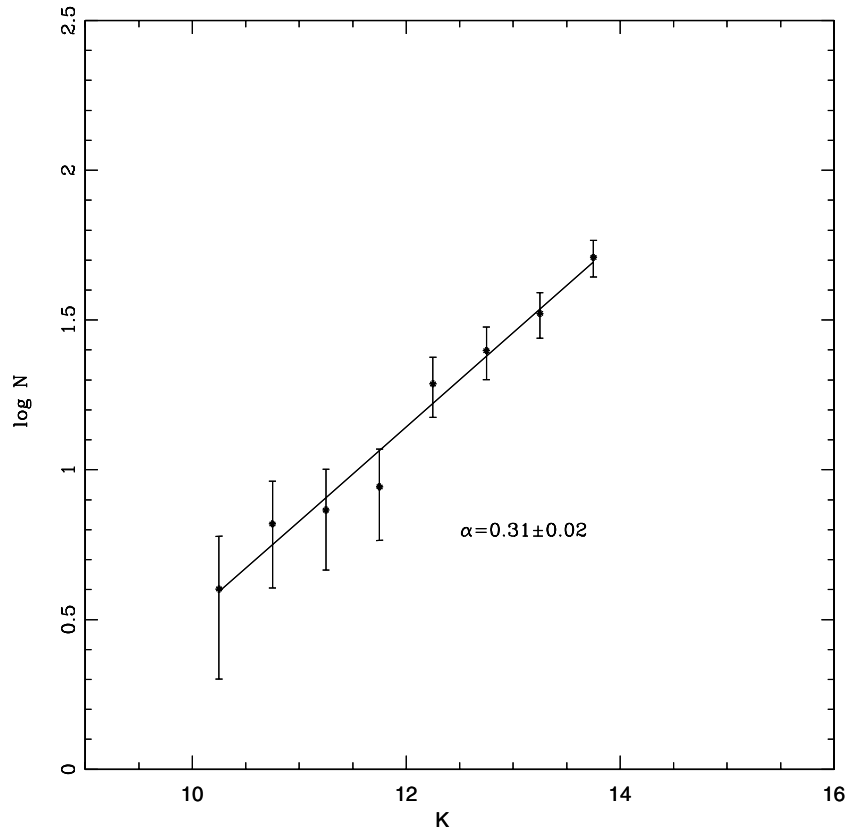
Figure 18. KLF derived after subtracting the model corrected field star contamination (see the text). The linear fit is represented by the continuous line.

$\sim$21 kpc which indicates that CC 14 is not associated with the IC 417 region. However, the distribution of NIR-excess and Hα emission stars shown in Fig. 19 seems to indicate a physical relationship between CC 14 and the H II region IC 417, which is discussed later. In Fig. 20 we show the RDP for CC 14 obtained from the 2MASS data around the position mentioned above, which indeed manifests a clustering with a radius of $\sim$1.5 arcmin.

In Fig. 21(a) we show $(J - H)/(H - K)$ CC diagram for stars in CC 14 cluster as well as for the YSOs distributed along the Nebulous Stream. A comparison of Fig. 21(a) with Fig. 12 indicates that the stars having $(J - H) > 0.6$ can be considered as probable YSOs associated with CC 14 and the Nebulous Stream. Assuming that the YSOs have average mass of $\sim$1 M$_\odot$ (i.e. $M_V \sim 4.5$ at 1 Myr), mean $V \sim 18.5$ mag and average $A_V \sim 2.5$ mag (cf. Fig. 21), we estimate a true distance modulus of $\sim$11.5, which clearly indicates that CC 14 and YSOs associated with the Nebulous Stream cannot be located at the distance ($\sim$21 kpc) suggested by Ivanov et al. (2005).

Of the 23 stars located within CC 14 region, the location of 10 stars (open circles) on the $(J - H)/(H - K)$ CC diagram indicates that they may be probable field stars. The RDP (Fig. 20) for CC 14 also indicates the presence of $\sim$14 field stars in the region. Probable members of CC 14 are shown by filled circles in Fig. 21(a). Figs 21(b) and (c) show $V/(V - I)$ and $J/(J - H)$ CMDs for the CC 14 region where open and filled circles represent field and probable cluster populations, respectively. Comparison of $V/(V - I)$ CMD (Fig. 21b) with the field region $V/(V - I)$ CMD (Fig. 8c) clearly indicates that the field population (open circles) in the embedded cluster region belongs to the same population as that of the nearby field region. The probable cluster members (filled circles) follow $\sim$1-Myr isochrone. In Figs 21(a)–(c) we have also plotted the NIR-

excess and Hα emission stars lying along the Nebulous Stream using crosses and star symbols, respectively. The $V/(V - I)$ CMD indicates that the stars lying on the Nebulous Stream also have ages of $\sim$1 Myr.

10 DISTRIBUTION OF GAS AND DUST AROUND STOCK 8

No detailed observations have been made so far, to probe the molecular cloud associated with Stock 8. Only available is the ^{12}CO contour map of IC 417 (Sh2-234) region traced from fig. 27(c) of Leisawitz, Bash & Thaddeus (1989), which is shown in Fig. 19. Although the resolution is low, a moderate-sized molecular cloud of $\sim$3.4 $\times$ 10^3 M$_\odot$ is found adjacent to the east of Stock 8.

In Fig. 19, NVSS (1.4-GHz) radio contours (white) and *MSX A*-band MIR contours (black) are overlaid on DSS-2 *R*-band image. The radio continuum emission peaks around $\alpha_{2000} \sim 05^h28^m18^s$ and $\delta_{2000} \sim +34°25'30''$ and shows a sharp cut-off at $\alpha_{2000} \sim 05^h28^m30^s$ indicating an interface between the ionized gas and molecular cloud. The integrated flux density of the radio continuum above 3σ level is estimated to be 2.474 Jy. Assuming a spherical symmetry for the ionized region and neglecting absorption of ultraviolet (UV) radiation by dust inside the H II region, the above flux density together with assumed distance, allow us to estimate the number of Lyman continuum photons (N_{Lyc}) emitted per second, and hence the spectral type of the exciting star. Using the relation given by Martín-Hernández, van der Hulst & Tielens (2003) and assuming an electron temperature of 8000 K, we estimated log $N_{Lyc} = 47.67$, which corresponds to a MS spectral type of $\sim$B0 (Panagia 1973; Schaerer & de Koter 1997). This seems to be consistent with the B0/O9.5 star
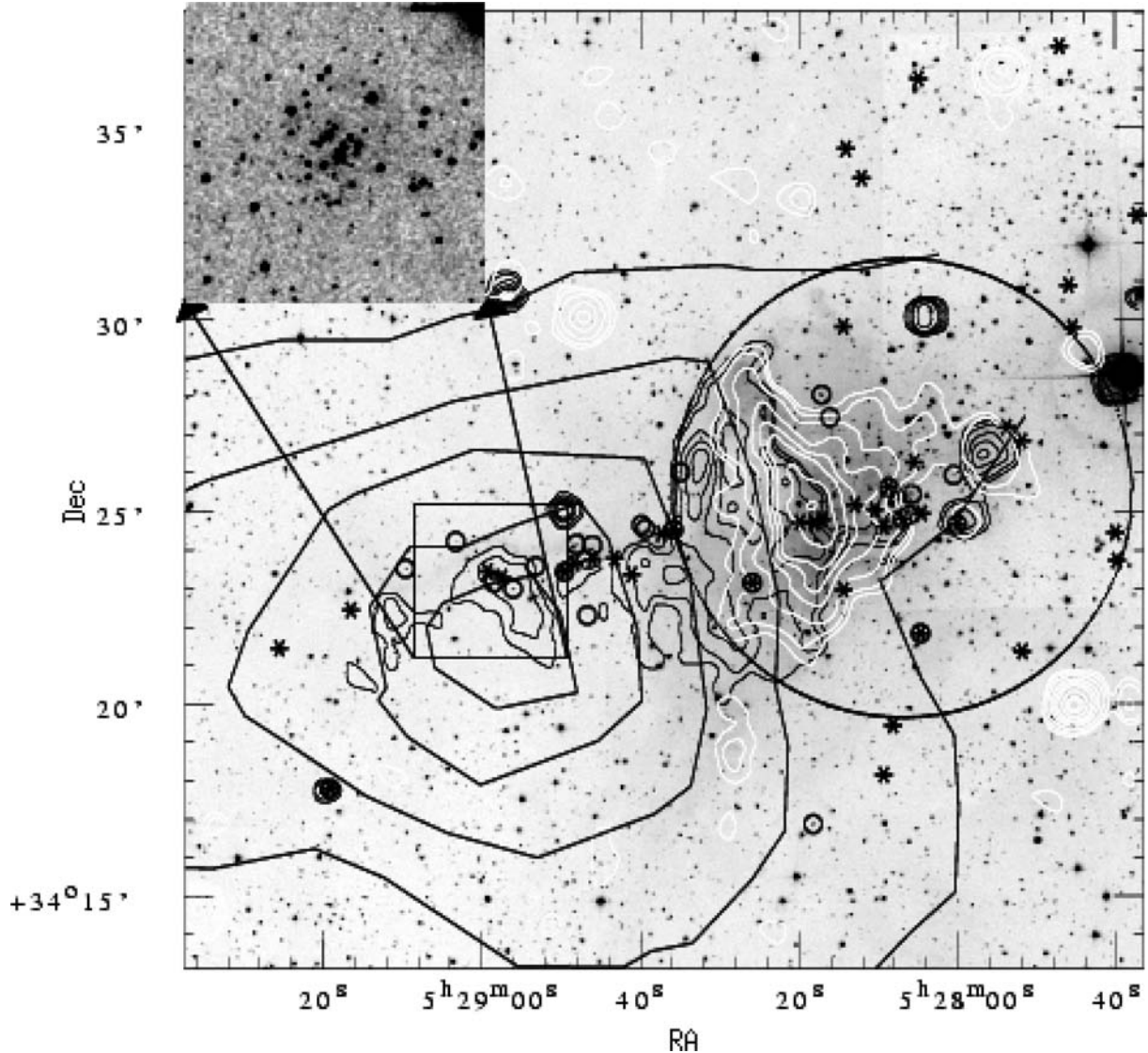
Figure 19. Spatial distributions of *Hα* emitters (open circles) and IR-excess sources (asterisk symbols) overlaid on DSS-2 *R*-band image. The thick contours represent ^{12}CO emission from Leisawitz et al. (1989). NVSS (1.4-GHz) radio contours (white) and *MSX A*-band intensity contours (thin black) have also been shown. The *MSX A*-band contours are 1.5, 2, 3, 4, 5, 10, 20, 40, 60, 80 per cent of the peak value 9.666×10^{-5} W m^{-2} Sr^{-1} and the NVSS radio contours are 3, 5, 10, 20, 40, 60, 80, 90 per cent of the peak value 29.5 mJy beam^{-1}. The circle having radius, $r = 6$ arcmin represents optical extent of the cluster (see Fig. 4). The inset box shows the enlarged 2MASS K_s-band image of the embedded cluster CC 14. The abscissa and the ordinates are for the J2000 epoch.

(cf. Table 3, star 1), at the centre of Stock 8, as the ionizing source of the region. Major uncertainty in the above calculation may arise due to neglect of the absorption of Lyman continuum photons by the dust. We estimated the effect of dust using the following two methods; 1) the dust continuum density was estimated by averaging far-infrared (FIR) optical depth τ_{100} (shown in Fig. 25a) over the radio emission region, and 2) attributing the spread in $E(B - V)$ in the cluster region (cf. Section 5) to the local dust distribution. In both the cases, we assumed a uniform dust distribution and the dust composition to be an equal mixture of silicate and graphite with properties identical to those given by Draine & Lee (1984). The calculation yields $\log N_{\text{Lyc}} \sim 48.15$ (from method 1) and 48.32 (from method 2) implying the ZAMS spectral type of the ionizing star to be O9/O8.5 and O8 from methods 1 and 2, respectively. Keeping in mind the uncertainties in estimating the spectral type of the star and the assumptions made to calculate the total number of Lyman continuum flux, we feel that the above estimates are comparable.

However, star 1 is located almost at the western edge of the ionized gas, so roughly half of its UV emission may not be used in creating the H II region. The H II region IC 417 contains several OB stars (cf. Mayer & Macak 1971), whose distribution is shown in Fig. 22. Presumably these stars are the first generation of stars in the IC 417 region. The details of the OB stars are given in Table 6. We suspect that the O8 and O9 stars (star Nos. 2 and 3, respectively), which jointly emit Lyman continuum photons of $\log N_{\text{Lyc}} = 48.78$, also contribute to ionize the IC 417 H II region to a similar extent of that by B0/O9.5 star in Stock 8, although they are located relatively far away.

The emission from *MSX A* band is completely absent from the inner region ($r < 2$ arcmin) as well as from the western region of Stock 8. It is stronger and more extended towards the eastern side of the cluster and then protrudes further to the east, nicely following the Nebulous Stream and showing a slight enhancement around CC 14. This further supports the physical connection between the H II
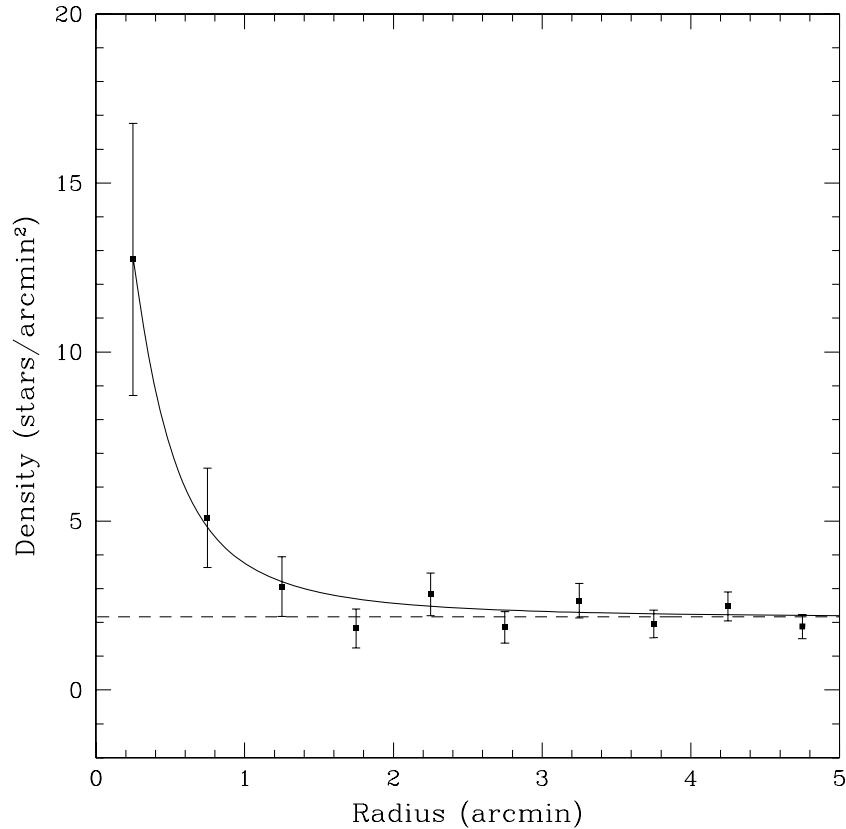
Figure 20. RDP for the embedded cluster CC 14 obtained from the 2MASS data. The continuous curve is the least-squares fit of the King (1962) profile to the observed data points and the error bars represent $\pm\sqrt{N}$ errors. The dashed line represents the mean density level of the field stars.
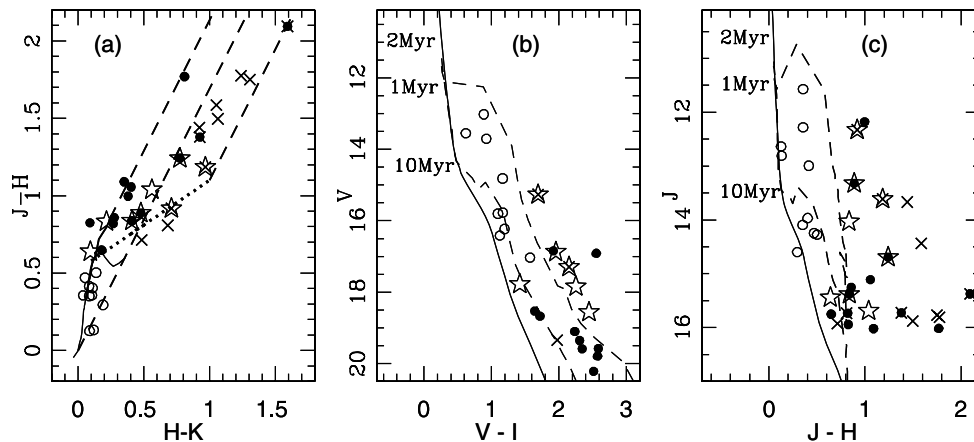
Figure 21. CC diagram and CMDs for the stars lying within 1.5 arcmin radius of the embedded cluster (CC 14 as well as for YSOs lying along the Nebulous Stream. (a) $(J − H)/(H − K)$ CC diagram with probable cluster members $(J − H > 0.6)$ as filled circles and field stars as open circles. Crosses and star symbols are the NIR-excess and Hα-emitting sources, respectively, lying along the Nebulous Stream. (b) and (c) are $V/(V − I)$ and $J/(J − H)$ CMDs, respectively. The symbols are same as in Fig. 21(a). In Figs 21(b) and (c) the isochrone of 2 Myr (continuous curve) by Girardi et al. (2002) and PMS isochrones of age 1 and 10 Myr (dashed curves) by Siess et al. (2000), corrected for cluster distance and reddening, are also shown.

region and the Nebulous Stream/CC 14. We show the *MSX A*-, *C*-, *D*- and *E*-band contour maps of the Stock 8 region in Fig. 23. The contours of the *MSX A* and *C* bands show an elliptical ridge around $\alpha_{2000} \sim 05^\mathrm{h}28^\mathrm{m}26^\mathrm{s}$, $\delta_{2000} \sim +34°25'00''$. The eastward contours seen in *A* (8 μm) and *C* (12 μm) bands lie beyond the ionization front and get diluted as we move towards *D* (15 μm) and *E* (21 μm)

bands, whereas the emission towards the west remains present in all the four bands. The emission in the MIR bands traces presence of warm small dust grains. The bands *A* and *C* also include several PAH features as described in Section 3. The morphology of the emission shown in Fig. 23 suggests that the westward emission may be due to warm small dust grains, whereas eastward emission in *A* and
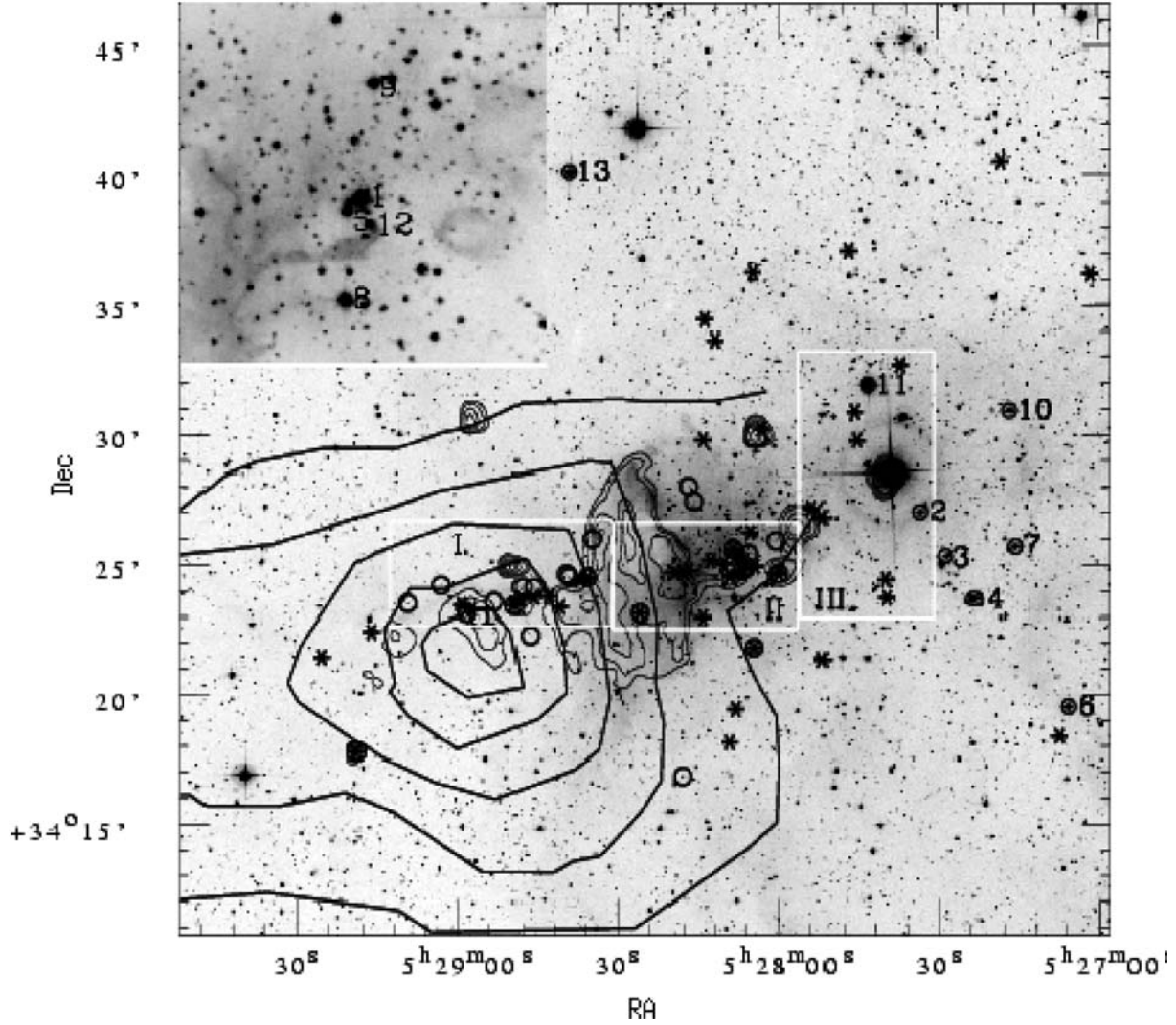
Figure 22. Spatial distributions of OB stars, Hα emitters (open circles) and IR-excess sources (asterisks) overlaid on DSS-2 *R*-band image of Stock 8 region. The inset box shows an enlarged view of 6 arcmin central region of Stock 8. The thick contours represent ^{12}CO emission from Leisawitz et al. (1989). *MSX A*-band intensity contours (thin lines) have also been shown. The contour levels are the same as in Fig. 19. The star numbers from Table 3 and three subregions (I–III, see the text) are also shown.

C bands may be due to PAHs because PAHs cannot survive in ionized regions as the hard radiation field within H II regions destroys them (Cesarsky et al. 1996).

In Fig. 24 we show *IRAS*-HIRES intensity maps for the cluster region at 12, 25, 60 and 100 μm. The emission at FIR (60 and 100 μm) peaks at $\alpha_{2000} \sim 05^h28^m24^s$; $\delta_{2000} \sim +34°24'00''$, whereas at MIR (25 μm) the emission peaks at $\alpha_{2000} \sim 05^h28^m10^s$; $\delta_{2000} \sim +34°25'30''$. The peaks of FIR and MIR emissions are ~2 arcmin away from the peak of the radio continuum emission, which indicates an interaction between the gas and dust around the region. *IRAS*-HIRES maps at 60 and 100 μm were also used to generate the spatial distribution of dust colour temperature [T(60/100)] and optical depth maps at 100 μm (τ_{100}) using the procedure given by Ghosh et al. (1993). An emissivity law of $\epsilon_\lambda \propto \lambda^{-1}$ was assumed to generate the optical depth map. Fig. 25 presents the contour maps of dust colour temperature [$T(60/100)$] and optical depth (τ_{100}). The dust colour temperature varies from 34 to 48 K as can be inferred from the map shown in Fig. 25. The relatively high temperature around the cluster may probably be due to the radiation from mas-

sive star(s) in the region. The τ_{100} map represents low optical depth around the position of Stock 8, whereas its peak matches well with the CO peak and the position of CC 14.

11 NATURE OF THE NEBULOUS STREAM

What is the nature of the Nebulous Stream? At first impression it appears like a giant Herbig–Haro jet and reminds us of HH 399 in Trifid nebula (Yusef-Zadeh, Biretta & Wardle 2005). However, this does not seem to be the case. Fig. 19 reveals that it is closely associated with the distribution of the *MSX A*-band emission, as well as the distribution of Hα emission stars and IR-excess stars. The cluster CC 14 is also embedded within the Nebulous Stream. We therefore interpret the Nebulous Stream as a bright rim or an ionization front.

Fig. 26 shows continuum-subtracted Hα and [S II] images for the region along with contours for *MSX A*-band emission and radio continuum superimposed on the [S II] image. The gap seen at the middle of Fig. 26 is because the field was observed in two frames
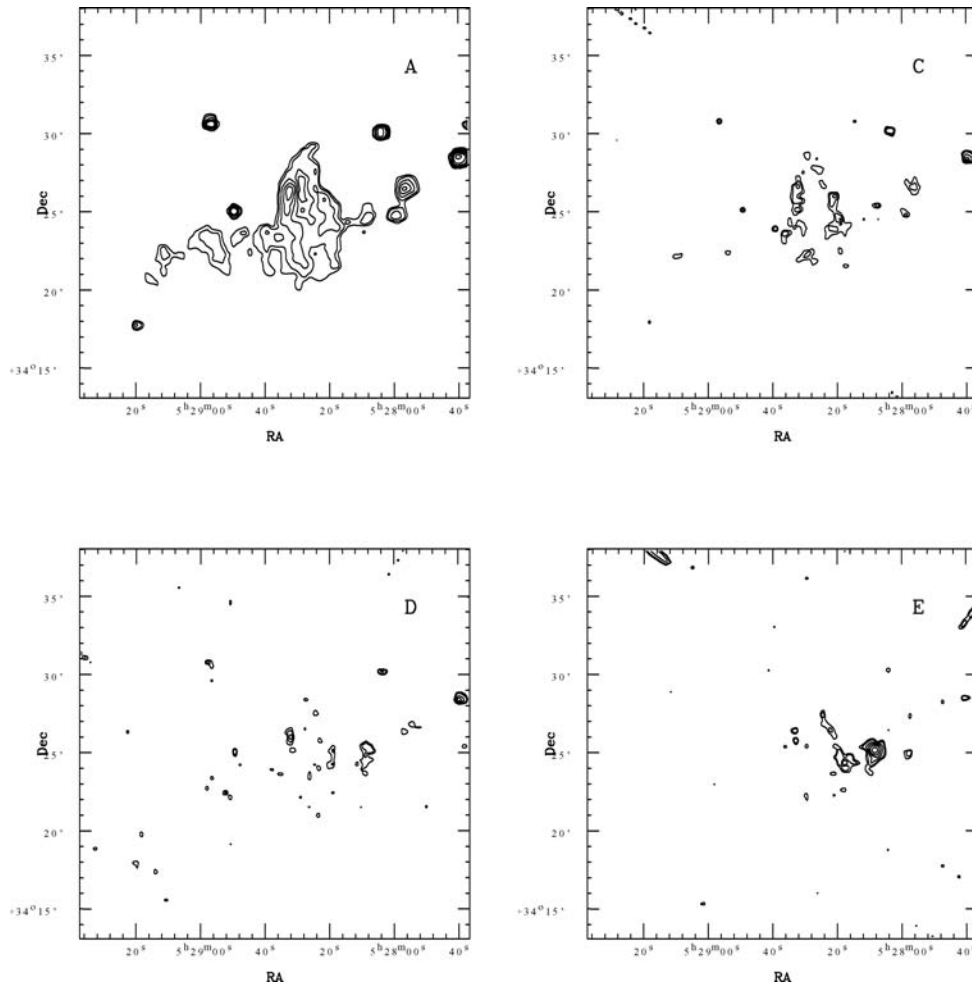
Figure 23. Top left-hand panel: *MSX A*-band intensity contours with levels as 80, 60, 40, 20, 10, 5, 4, 3, 2, 1.5 per cent of the peak value 9.666×10^{-5} W m^{-2} Sr^{-1}. Top right-hand panel and bottom left-hand panel: *C*- and *D*-band intensity contours with levels as 90, 80, 60, 40, 20, 15, 12 per cent of the peak value 1.218×10^{-5} W m^{-2} Sr^{-1} and 7.239×10^{-6} W m^{-2} Sr^{-1}, respectively. Bottom right-hand panel: *E*-band intensity contours with levels as 90, 80, 70, 60, 50, 40, 35 per cent of the peak value 6.298×10^{-6} W m^{-2} Sr^{-1}. The abscissa and ordinates are in J2000 epoch.

without an overlap. The Hα emission is more extended compared to the [S II] emission. The [S II] emission comes from low-excitation zones and is enhanced close to the ionization fronts (cf. Deharveng et al. 2003). Therefore the spatial distribution of the [S II]/Hα ratio should give information on the excitation conditions. The variation of the [S II]/Hα ratio along a 0.5 arcmin wide strip (indicated by black dashed lines in Fig. 26) as a function of radial distance from Stock 8 is shown in Fig. 27. To improve the S/N and to remove faint stars, the images were median filtered using a 3 × 3 pixel box. A background was then determined for these smoothed images by calculating the statistics inside a 3 × 3 pixel box at various places where the Hα and [S II] brightness is at a minimum. The average background value was then subtracted from each pixel. As can be seen in Fig. 27 the ratio of [S II]/Hα is higher eastwards of the cluster Stock 8. Note that the values in the easternmost region are not reliable because the error bars are very large. Mean value of the [S II]/Hα ratio for the central region $r < 6$ arcmin of Stock 8 is ~0.18 ± 0.06, which is consistent with the ratio expected for an H II region associated with a late O-B0 type star (Reynolds 1988). However, in the region between 7 and 12 arcmin the mean value of the ratio is higher, ~0.24 ± 0.02. This indicates that the Nebulous Stream

is a low-excitation object suggestive of its bright rim/ionization front nature.

The question then arises: where is (are) the source(s) of its excitation? The O9.5/B0 stars of Stock 8 or O8/O9 stars further west do not seem to be the possible source because the morphology of the radio and *MSX A*-band emissions indicates an interface at $\alpha_{2000} \sim 05^h 28.5^m$ and suggests that the ionization front has not reached the Nebulous Stream. UV radiation from the west of the Stream is most probably blocked by the molecular gas located at the interface at $\alpha_{2000} \sim 05^h 28^m 5$. In addition, the Stream runs in the east–west direction, which suggests that the UV photons responsible for the Stream should arrive from the north. In a search towards the north of the Stream, we find an O8 star (star number 13 at $\alpha_{2000} = 05^h 28^m 39^s$, $\delta_{2000} = +34°40'09''$, distance ~2.06 kpc: Cruz-Gonzalez et al. 1974; 2.7 kpc: Savage et al. 1985) located at a projected distance of 9 pc from the Nebulous Stream. We suspect that this star could be the possible source of UV photons which excite the Stream.

In order to verify whether this star emits enough UV photons to generate the bright rim, we calculated the flux of Lyman continuum photons which are expected to arrive at the location of the bright
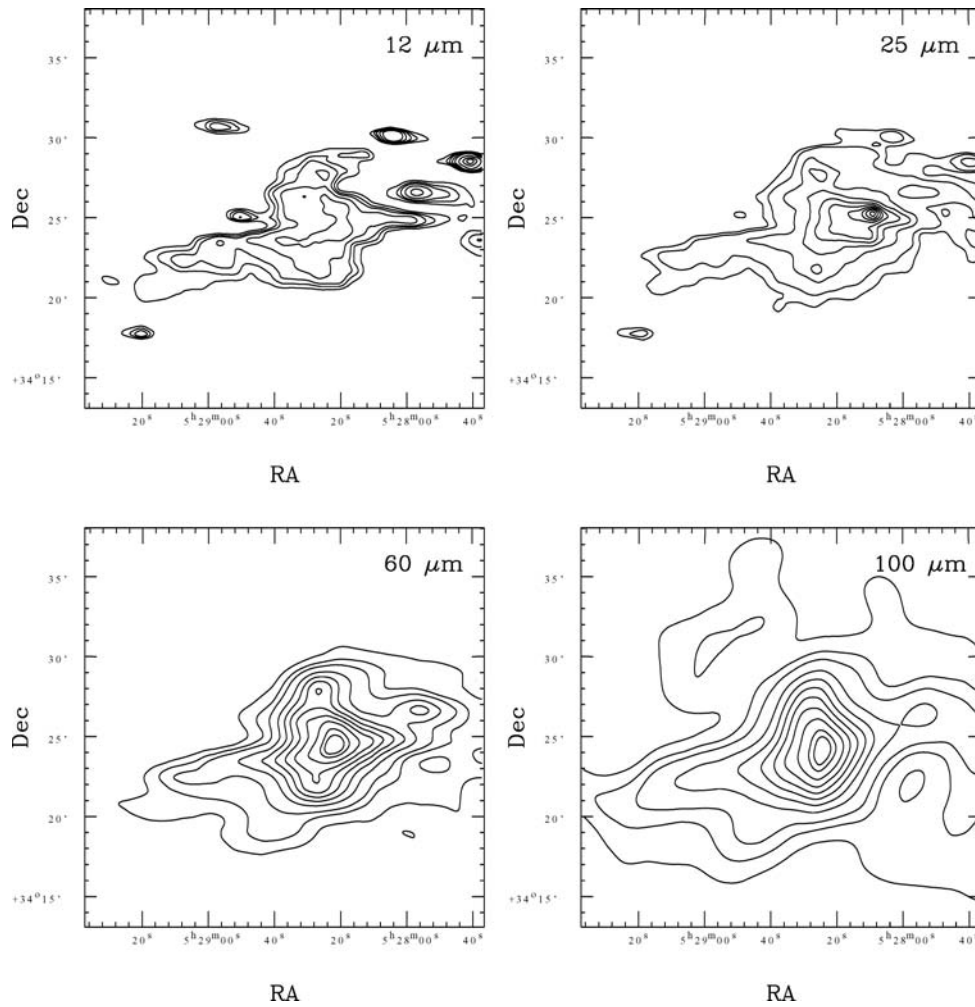
Figure 24. *IRAS*-HIRES intensity maps of 12 μm (top left-hand panel), 25 μm (top right-hand panel), 60 μm (bottom left-hand panel) and 100 μm (bottom right-hand panel). The contours are at 3, 4, 5, 7, 10, 20, 40, 60, 80, 90 per cent of the peak value of 190.5 MJy Sr^{-1} at 12 μm; 7, 10, 20, 30, 40, 50, 60, 70, 80, 90 per cent of the peak value of 97.7 MJy Sr^{-1} at 25 μm; 10, 15, 20, 30, 40, 50, 60, 70, 80, 90, 95 per cent of the peak values of 332.6 MJy Sr^{-1} and 515.4 MJy Sr^{-1} at 60 and 100 μm, respectively. The abscissa and ordinates are in J2000 epoch.
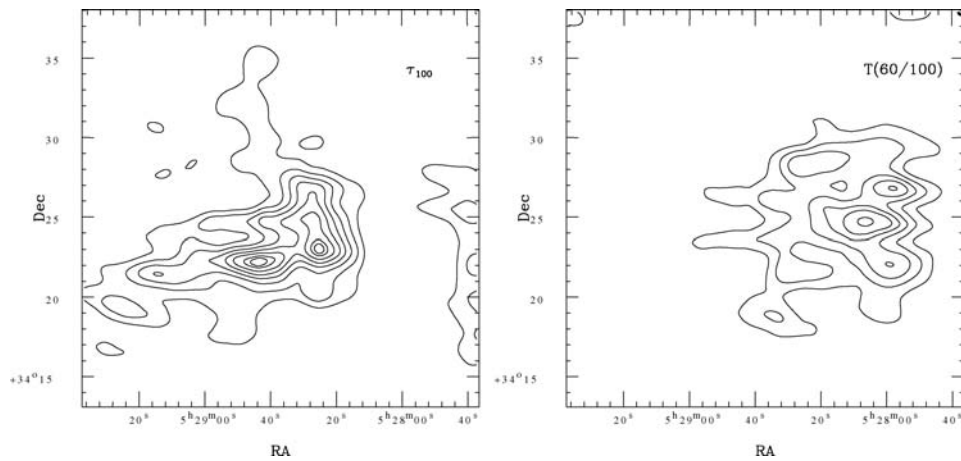
Figure 25. Left-hand panel: The dust optical depth (τ_{100} at 100 μm) distribution of the region around the cluster. The contours are at 30, 40, 50, 60, 70, 80, 90, 95 per cent of the peak value 6.85×10^{-4}. Right-hand panel: Dust colour temperature map of the region around the cluster. The contour levels are at 34, 36, 39, 42, 44, 48 K.
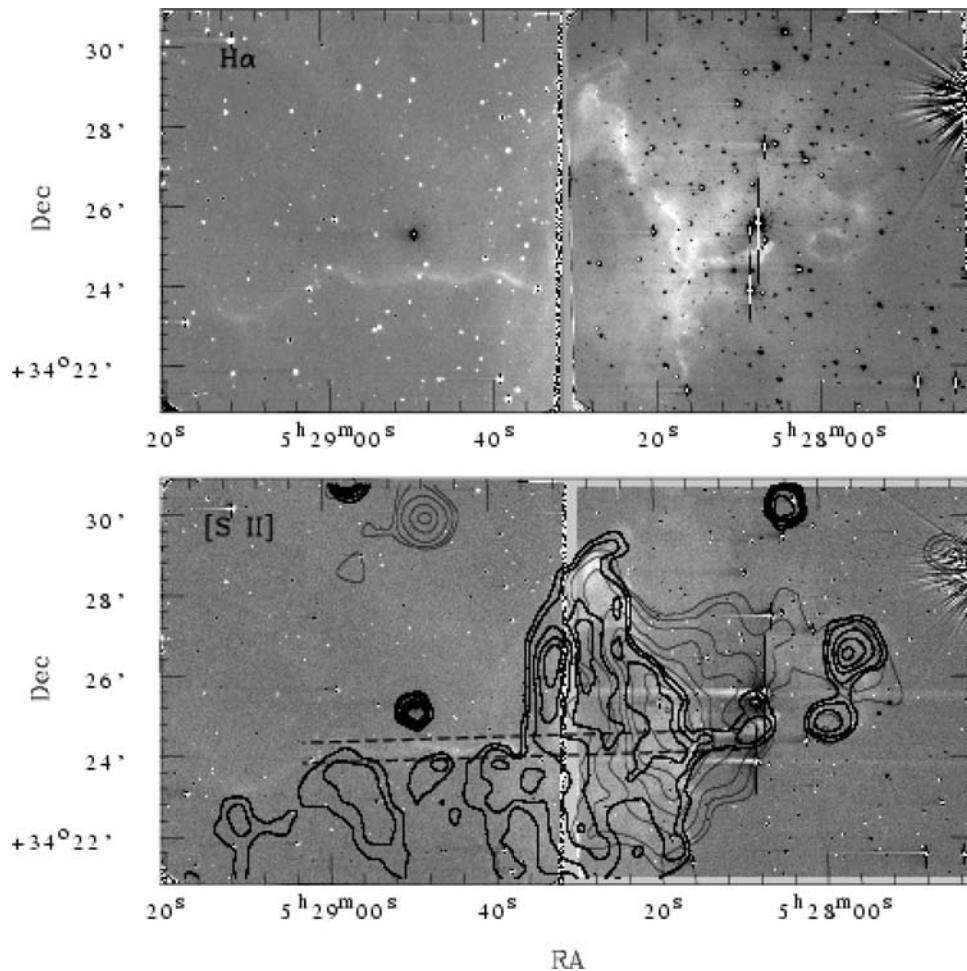
Figure 26. A Continuum-subtracted (20×10 arcmin^2) Hα (upper panel) and [S II] (lower panel) images of the regions around Stock 8 overlaid with *MSX A*-band contours (thick black) and NVSS radio continuum contours (light black). The contour intensity levels are the same as mentioned in Fig. 19. The abscissa and the ordinates are for the J2000 epoch. The discontinuity in the images at $\alpha_{2000} \sim 05^h28^m30^s$ is an artefact of observations as the region shown in the figure is mosaic of two non-overlapping frames. The area between dashed lines represents a 0.5 arcmin wide strip along the Nebulous Stream (see text). Spatial variation of [S II]/Hα ratio along the strip is shown in Fig. 27.

rim. The flux associated with an O8 star is taken from Panagia (1973). We assumed in our calculations, that loss of photons due to absorption by interstellar matter between the star and bright rim is negligible. Using a projected distance of $\sim$9 pc between the star and the bright rim, the Lyman photon flux at the bright rim is estimated to be $\sim 4 \times 10^8$ cm^{-2} s^{-1}. The Lyman photon flux reaching a radial distance of 6 arcmin ($\sim$3.6 pc) from B0 star is $\sim 2.7 \times 10^8$ cm^{-2} s^{-1}. The estimated flux of $\sim 4 \times 10^8$ cm^{-2} s^{-1} in the case of O8 star is comparable to the ionizing flux associated with the bright-rimmed clouds (see Morgan et al. 2004; Thompson, Urquhart & White 2004) which supports an O8 star as responsible for the Nebulous Stream.

12 STAR FORMATION SCENARIO IN THE VICINITY OF STOCK 8

The energetic stellar UV radiation and winds from massive stars could disperse nearby clouds and consequently terminate further star formation. Alternatively, they can enhance star formation activity in the region. Elmegreen & Lada (1977) proposed that after formation of massive stars, the expanding ionization fronts play a constructive role in inducing a sequence of star formation activities in the neighbourhood. The distribution of visible young stars and embedded YSOs and the morphological details of the environment around the cluster containing OB stars can be used to probe the star formation history of the region.

In addition to the ^{12}CO contours and the locations of OB stars, Fig. 22 also shows spatial distribution of NIR-excess sources and Hα emission stars. In Fig. 28 we plot NIR excess, $\Delta(H - K)$, for three subregions (regions I–III) shown in Fig. 22 as a function of radial distance from the centre of the cluster Stock 8. Fig. 28 indicates that the stars lying in regions I and III show relatively higher NIR excess. This trend in NIR excess may be an indication of the youth of YSOs located in regions I and III as compared to those located near the centre of Stock 8. To verify further the age sequence, we plot $V/(V - I)$ and $K/(H - K)$ CMDs for the three subregions in Fig. 29, which also suggests that the YSOs in regions I and III are relatively younger than those located near the cluster centre.

As mentioned earlier, several OB stars are located around the cluster Stock 8. We suspect that these sources belong to the first generation of stars formed in the IC 417 region, although the evidence is rather weak because of their scattered distribution. The age of the early-type stars in Stock 8 is estimated to be $\leqslant$2 Myr, whereas the YSOs in the Stock 8 region indicate an average age of

---

Figure 29. $V/(V − I)$ and $K/(H − K)$ CMDs for the Hα (triangles) and NIR-excess sources (circles) lying in three subregions as shown in Fig. 22. The isochrone of 2 Myr (continuous curve) by Girardi et al. (2002) and PMS isochrones (dashed curves) for ages 0.5, 5 and 10 Myr by Siess et al. (2000) corrected for cluster distance and reddening are also shown.

region of the cluster is ionization bounded; whereas, the western region of the Stock 8 is density bounded. The morphology of radio emission and *MSX A*-band emission suggests that ionization/shock front caused by the central ionization source of Stock 8 and by O-type stars located in the western region of Stock 8 has not reached the Nebulous Stream. An O8 star located ∼9 pc away towards the north of the Nebulous Stream may be a probable source of the bright-rimmed Nebulous Stream.

The slope of the MF Γ in the mass range $\sim 1.0 \leqslant M/M_\odot < 13.4$ can be represented by -1.38 ± 0.12, which agrees well with Salpeter value (-1.35). In the mass range $0.3 \leqslant M/M_\odot < 1.0$ the MF is found to be shallower with $\Gamma = -0.58 \pm 0.23$ indicating a break in the slope of the MF at $\sim 1\,M_\odot$. The slope of the KLF for the cluster is found to be 0.31 ± 0.02 which is smaller than the average value (~ 0.4) obtained for young star clusters (Lada et al. 1991; Lada & Lada 1995, 2003).

REFERENCES

Adams F. C., Lada C. J., Shu F. H., 1987, ApJ, 312, 788
Aumann H. H., Fowler J. W., Melnyk M., 1990, AJ, 99, 1674
Bertout C., Basri G., Bouvier J., 1988, ApJ, 330, 350
Bessell M. S., Brett J. M., 1988, PASP, 100, 1134

Borissova J., Pessev P., Ivanov V. D., Saviane I., Kurtev R., Ivanov G. R., 2003, A&A, 411, 83

Brandl B., Brandner W., Eisenhauer F., 1999, A&A, 352, L69

Carraro G., Vzquez R. A., Moitinho A., Baume G., 2005, ApJ, 630, L153

Cesarsky D., Lequeux J., Abergel A., Perault M., Palazzi E., Madden S., Tran D., 1996, A&A, 315, L305

Chen H., Tafalla M., Greene T. P., 1997, ApJ, 475, 163

Chen L., de Grijs R., Zhao J. L., 2007, AJ, 134, 1368

Chini R., Krugel E., 1983, A&A, 117, 289

Chini R., Wargau W. F., 1990, A&A, 227, 213

Cohen J. G., Frogel J. A., Persson S. E., Ellias J. H., 1981, ApJ, 249, 481

Cruz-Gonzalez C., Recillas-Cruz E., Costero R., Peimbert M., Torres-Peimbeert S., 1974, Rev. Mex. Astron. Astrofis., 1, 211

Cutri R. M. et al., 2003, The IRSA 2MASS All-Sky Point Source Catalog. NASA/IPAC Infrared Science Archive (http://irsa.ipac.caltech.edu/applications/Gator/)

Damiani F., Micela G., Sciortino S., Hulamo N., Moitinho A., Harnden F. R., Jr., Murray S. S., 2006, A&A, 460, 133

de Grijs R., Gilmore G. F., Johnson R. A., Mackey A. D., 2002a, MNRAS, 331, 228

de Grijs R., Gilmore G. F., Johnson R. A., Mackey A. D., 2002b, MNRAS, 331, 245

de Grijs R., Gilmore G. F., Mackey A. D., Wilkinson M. I., Beaulieu S. F., Johnson R. A., Santiago B. X., 2002c, MNRAS, 337, 597

Deharveng L., Zavagno A., Salas L., Porras A., Caplan J., Cruz-Gonzalez I., 2003, A&A, 399, 1135

Dolan C. J., Mathieu R. D., 2002, AJ, 123, 387

Draine B. T., Lee H. M., 1984, ApJ, 285, 89

Elmegreen B. G., Lada C. J., 1977, ApJ, 214, 725

Fischer P., Pryor C., Murray S., Mateo M., Richtler T., 1998, AJ, 115, 592

Georgelin Y. M., Georgelin Y. P., Roux S., 1973, A&A, 25, 337

Ghosh S. K., Verma R. P., Rengarajan T. N., Das B., Saraiya H. T., 1993, ApJS, 86, 401

Girardi L., Bertelli G., Bressan A., Chiosi C., Groenewegen M. A. T., Marigo P., Salasnich B., Weiss A., 2002, A&A, 391, 195

He L., Whittet D. C. B., Kilkenny D., Spencer Jones J. H., 1995, ApJS, 101, 335

Hillenbrand L. A., 1997, AJ, 113, 1733

Hillenbrand L. A., Strom S. E., Vrba F. J., Keene J., 1992, ApJ, 397, 613

Hillenbrand L. A., Massey P., Strom S. E., Merrill K. M., 1993, AJ, 106, 1906

Ivanov V. D., Borissova J., Bresolin F., Pessev P., 2005, A&A, 435, 107

Johnson H. L., 1966, ARA&A, 4, 193

Johnson H. L., Morgan W. W., 1953, ApJ, 117, 313

King I., 1962, AJ, 67, 471

Kroupa P., 2001, MNRAS, 322, 231

Kroupa P., 2002, Sci, 295, 82

Kroupa P., 2007, in Knapen J. H., Mahoney T. J., Vazdekis A., eds, Pathways Through an Eclectic Universe, preprint (astro-ph/0708.1164)

Lada E. A., Lada C. J., 1995, AJ, 109, 1682

Lada C. J., Lada E. A., 2003, ARA&A, 41, 57

Lada E. A., Evans N. J., Depoy D. L., Gatley I., 1991, ApJ, 371, 171

Lada C. J., Muench A. A., Rathborne J. M., Alves J. F., Lombardi M., 2008, ApJ, 672, 410

Landolt A. U., 1992, AJ, 104, 340

Larson R. B., 1992, MNRAS, 256, 641

Lee H. T., Chen W. P., Zhang Z. W., Hu J. Y., 2005, ApJ, 624, 808

Leisawitz D., Bash F. N., Thaddeus P., 1989, ApJS, 70, 731

Leistra A., Cotera A. S., Leibert J., Burton M., 2005, AJ, 130, 1719

Luhman K. L., Rieke G. H., Young E. T., Cotera A. S., Chen H., Rieke M. J., Scheider G., Thompson R. I., 2000, ApJ, 540, 1016

Malysheva L. K., 1990, SvA, 34, 122

Martín-Hernández N. L., van der Hulst J. M., Tielens A. G. G. M., 2003, A&A, 407, 957

Massey P., Johnson K. E., Degio-Eastwood K., 1995, ApJ, 454, 151

Mayer P., Macak P., 1971, Bull. Astron. Czech., 22, 46

Megeath S. T., Herter T., Beichman C., Gautier N., Hester J. J., Rayner J., Shupe D., 1996, A&A, 307, 775

Meyer M., Calvet N., Hillenbrand L. A., 1997, AJ, 114, 288

Morgan L. K., Thompson M. A., Urquhart J. S., White G. J., Miao J., 2004, A&A, 426, 535

Muench A. A., Lada E. A., Lada C. J., Alves J., 2002, ApJ, 573, 366

Muench A. A. et al., 2003, AJ, 125, 2029

Neckel Th., Chini R., 1981, A&AS, 45, 451

Ogura K., Sugitani K., 1998, Publ. Astron. Soc. Aust., 15, 91

Ojha D. K. et al., 2004a, ApJ, 608, 797

Ojha D. K. et al., 2004b, ApJ, 616, 1042

Panagia N., 1973, AJ, 78, 929

Pandey A. K., Mahra H. S., Sagar R., 1992, BASI, 20, 287

Pandey A. K., Ogura K., Sekiguchi K., 2000, PASJ, 52, 847

Pandey A. K., Nilakshi O. K., Sagar R., Tarusawa K., 2001, A&A, 374, 504

Pandey A. K., Upadhyay K., Nakada Y., Ogura K., 2003, A&A, 397, 191

Pandey A. K., Upadhyay K., Ogura K., Sagar R., Mohan V., Mito H., Bhatt H. C., Bhatt B. C., 2005, MNRAS, 358, 1290

Pandey A. K., Sharma S., Ogura K., 2006, MNRAS, 373, 255

Pandey A. K., Sharma S., Ogura K., Ojha D. K., Chen W. P., Bhatt B. C., Ghosh S. K., 2007, MNRAS preprint (arXiv:0710.5429)

Parker R. J., Goodwin S. P., 2007, MNRAS, 380, 1271

Preibisch T., Zinnecker H., 1999, AJ, 117, 2381

Price N. M., Podsiadlowski P., 1995, MNRAS, 273, 1041

Price S. D., Egan M. P., Carey S. J., Mizuno D. R., Kuchar T. A., 2001, AJ, 121, 2819

Prisinzano L., Damiani F., Micela G., Sciortino S., 2005, A&A, 430, 941

Reynolds R. J., 1988, ApJ, 333, 341

Robin A. C., Reyle C., Derriere S., Picaud S., 2003, A&A, 409, 523

Salpeter E. E., 1955, ApJ, 121, 161

Samal M. R., Pandey A. K., Ojha D. K., Ghosh S. K., Kulkarni V. K., Bhatt B. C., 2007, ApJ, 671, 555

Sanchawala K. et al., 2007, ApJ, 667, 963

Savage B. D., Massa D., Meade M., Wesselius P. R., 1985, ApJS, 59, 397

Scalo J., 1998, in Gilmore G., Howell D., eds, ASP Conf. Ser. Vol. 142, The Stellar Initial Mass Function. Astron. Soc. Pac., San Francisco, p. 201

Schaerer D., de Koter A., 1997, A&A, 322, 598

Sharma S., Pandey A. K., Ojha D. K., Chen W. P., Ghosh S. K., Bhatt B. C., Maheswar G., Sagar R., 2007, MNRAS, 380, 1141

Siess L., Dufour E., Forestini M., 2000, A&A, 358, 593

Stetson P. B., 1987, PASP, 99, 191

Tapia M., Roth M., Costero R., Echevarria J., Roth M., 1991, MNRAS, 253, 649

Thompson M. A., Urquhart J. S., White G. J., 2004, A&A, 415, 627

Wegner W., 1993, A&A, 43, 209

Winkler H., 1997, MNRAS, 287, 481

Yusef-Zadeh F., Biretta J., Wardle M., 2005, ApJ, 624, 246

SUPPLEMENTARY MATERIAL

The following supplementary material is available for this article:

Table 2. *UBVI*$_c$ photometric data of the sample stars.

This material is available as part of the online article from: http://www.blackwell-synergy.com/doi/abs/10.1111/j.1365-2966.2007.12825.x
(this link will take you to the article abstract).

Please note: Blackwell Publishing are not responsible for the content or functionality of any supplementary materials supplied by the authors. Any queries (other than missing material) should be directed to the corresponding author for the article.

This paper has been typeset from a TEX/LATEX file prepared by the author.